Investigation of Propagation Conditions along Earth-Space Links by Means of High Resolution Numerical Weather Predictions

Master of Science in Telecommunication Engineering

November 14, 2020

POLITECNICO
MILANO 1863

Candidate: Cameron McAinsh, 894190

Supevisor: Prof. Carlo Riva

Contents

List of Figures

List of Tables

Abstract

The increasing use of satellites has led to the saturation of lower frequency bands. Consequently new technological solutions are being investigated so that higher bands can be exploited by the next generation of communication systems, giving access to wider bandwidths. However high frequencies are subject to many tropospheric impairments, including absorption and scattering due to rain, clouds and gases. In this context, the study conducted in this thesis investigates the characterization and prediction of the tropospheric attenuation for high frequency Earth-space links using The Weather Research and Forecasting model (WRF). Specifically, the link between the Alphasat satellite and the ASI ground station located in Spino d'Adda was studied at the frequency of 19.7GHz.

The accurate characterization of the troposheric signal attenuation represents a main challenge for the design of new satellite communication systems.

1 Introduction

Next generations of satellite communication systems demand the use higher frequency bands [1]. There are three main reasons for this:

1. To accommodate a dramatic and continuous increase in data needs as the number of users who access multimedia services (data transfer, video, internet, etc.) has pushed development of new and rate-demanding applications.

2. Band congestion. System designers are always looking for ways to relieve congestion, and to avoid sharing and coordination problems that are present in certain frequency bands.

3. Certain frequency reuse techniques can be efficiently accomplished at higher frequencies.

Along with the increase in the operating frequency, a recent interest in building large low Earth orbiting (LEO) constellations of satellites on a new and larger scale, has created a need to be able to provide accurate prediction of the propagation impairments along fast moving slant paths.

The aim is to deliver Internet to the world by providing truly global and robust broadband coverage. Players such as OneWeb, SpaceX, Samsung, and Boeing all have proposals for such a system. Each plans on launching constellations of 600 to over 4000 satellites, dwarfing the 1400 operational satellites currently in orbit. This sheer number of satellites, along with their global coverage, gives rise to opportunities not only for broadband but also as a platform for providing navigation services [2].

In this context, the objective of this work is to take advantage of the Weather Research and Forecasting (WRF) system capable of providing reanalysis and forecasts at high resolution, which, in turn, can be used to predict the signal attenuation for slant path satellite links beyond 10 GHz.

1.1 Satellite Orbits and Congestion

There are three distinct regimes where satellites tend to reside. Low Earth orbiting (LEO) satellites are generally placed between 400 and 1500 km in altitude. Lower, and orbits decay too quickly due to atmospheric drag. Higher, and their lifetime is cut short from radiation exposure in the lower Van Allen belt [4]. At the other extreme are the geosynchronous (GEO) satellites just above 35,000 km. Designed with an orbital period that matches that of Earth, if placed at the equator these satellites reside in the same place in the sky. There is nearly an equal divide of the 1419 operational satellites in orbit today between LEO with 780 and GEO with 506. There is not much placed in the vast distance between, nearly three Earths apart. This is partly because radiation levels are high, demanding specialized hardened components. However, this is where we

find the 100 or so operational navigation satellites, nearly at the midpoint between LEO and GEO and hence in a medium Earth orbit (MEO). Figure shows LEO, MEO and GEO orbits.

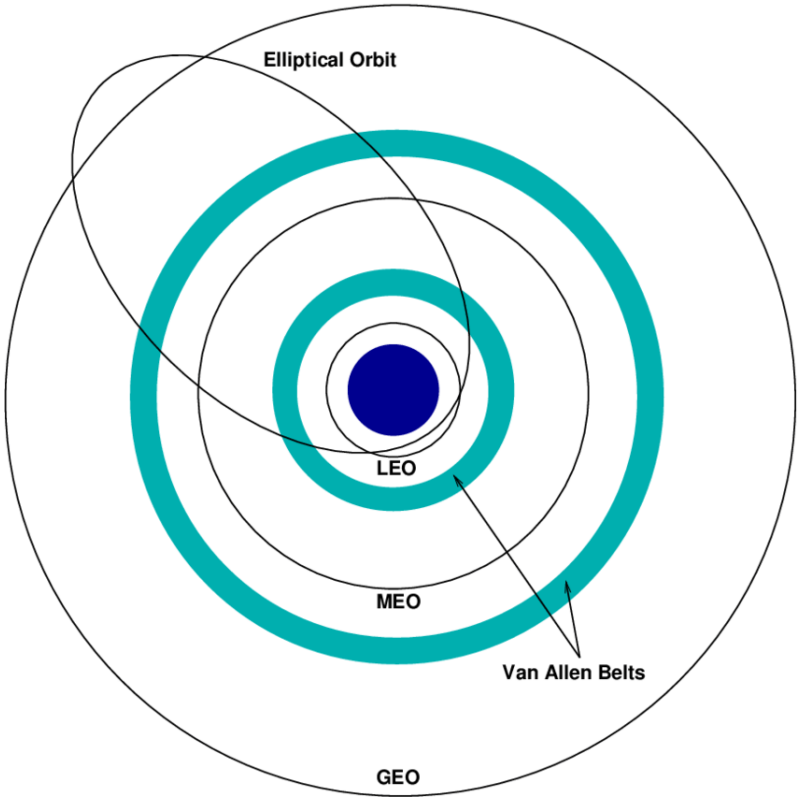

Figure 1: Satellite orbits

In late 2014 and early 2015, the International Telecommunications Union (ITU) reported a half dozen filings for spectrum allocation for large constellations of LEO satellites. In January 2015, OneWeb announced a partnership with Virgin and Qualcomm to produce a constellation of 648 LEO satellites to deliver broadband Internet globally. Within days of this announcement, SpaceX, with support from Google, announced a similar ambition for a constellation of over 4000 LEO satellites. In August of 2015, Samsung expressed interest with a proposal for a LEO constellation of 4600. Boeing joined the race in June of 2016 announcing plans for a LEO constellation of nearly 3000. These new LEO constellations are being proposed to keep up with the rising demand for broadband, not to replace ground infrastructure, but to allow us to keep up. From a more humanitarian perspective, these systems bring Internet access to the 54% of the population that do have the infrastructure today [3].

1.2 Context of the Investigation

Two independent Earth-space links will always encounter a different path, obstructions and atmospheric conditions. It is impossible to formulate an exact loss for all telecommunication systems in a single mathematical equation. Different models exist for different types of links under different conditions. Most models calculate the path loss for a link under a certain probability that the considered conditions will occur. Since atmospheric phenomena have a high degree of space-time variations, they should be incorporated in a stochastic analysis. This implies that most of the models are in fact empirical in nature, because they are developed based on large sets of data collected for given tropospheric conditions. Moreover, the influence of atmospheric conditions is significant for small percentages of time over a year, so that their accurate estimation is strictly related to the availability of the system, defined as the time percentage during a year that a specific parameter of the telecommunication link must be lower than a certain threshold, beyond which an outage of the satellite link occurs. This characteristic is studied by means of the CCDF (Complementary Cumulative Distribution Functions), which shows for a given frequency the probability that a given attenuation is exceeded. The Radio communication unit of the ITU provides official models for Satcom systems design purposes in the form of recommendations (named ITU-R) [6], approved by all the ITU member States. This work will make use of these recommendation to assess the impact of certain weather conditions on Earth-space links.

1.3 WRF and Software Implementation

The Weather Research and Forecasting (WRF) model is a state-of-the-art atmospheric modeling system designed for both meteorological research and numerical weather prediction [20]. This model allows to simulate several physical variables governing the state of the atmosphere on spatial and temporal resolutions sufficiently fine to allow their conversion into exploitable propagation data. Data such as temperature, pressure, humidity and wind profiles are downloaded across all pixels in space to cover the output grids of WRF. For each pixel, several tens of parameters are calculated.

Starting from the extraction of these parameters and by following ITU recommendations, the attenuation of certain atmospheric phenomena can be estimated through software. The meteorological data of the WRF model are therefore combined with this software. The software is independent of the WRF model allowing to convert the descriptive parameters of the atmosphere into propagation data and time series of propagation impairments. Post-processing is applied to some of the WRF outputs such as the pressure, the temperature and the mixing ratios of rain, on the basis of the propagation impairment under consideration. In the context of this study, we are interested in attenuation, and the WRF outputs are chosen accordingly, as we will see in following chapters. The implemented software is then used to analyze data across an extended period of time across multiple frequencies. The data is then compared against the

measurements collected in the framework of the Alphasat Aldo Paraboni propagation experiment, a joint collaboration between the Italian Space Agency (ASI) and the European Space Agency (ESA) [16].

2 Data

This chapter will introduce the two data sets used in this work.

2.1 NWP Models

NWP, numerical Weather predictions use computer simulations to predict the weather through numerical means. It can be used to predict future weather conditions or to recreate and reconstruct previous states of the atmosphere. NWP are numerically very intense, working through many processes and sub process at different temporal and spatial conditions. Depending on the spatial scale of analysis the models are categorized into Global or Regional models.

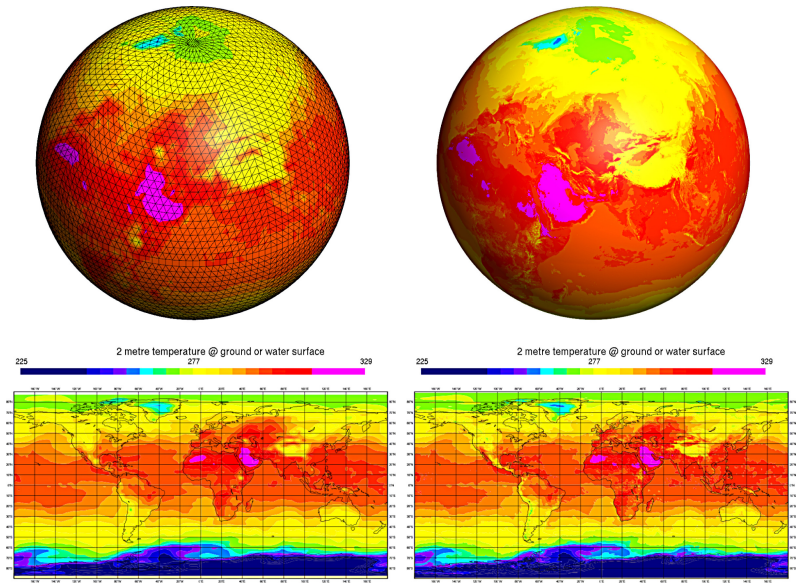

Figure 2: Global NWP model

Global NWP models consider the whole of Earth's atmosphere as in figure 2. Data from global models are important to set up initialization and boundary conditions for anyone running NWP at a regional level.

Regional NWP models, pictured in figure 3, are limited to a certain area of the Earth. In terms of simulation the modeling strategy is very different from the ones employed by global models. Regional domains do not benefit from the closed and periodic boundary conditions obtained by considering the entire globe. Therefore the boundary conditions have to be specified externally, and the most simple way to do this is to take the global NWP models themselves.

For this work a specific NWP model is used, the Weather Research and Forecasting (WRF) software by NCAR (National Center for Atmospheric Research).

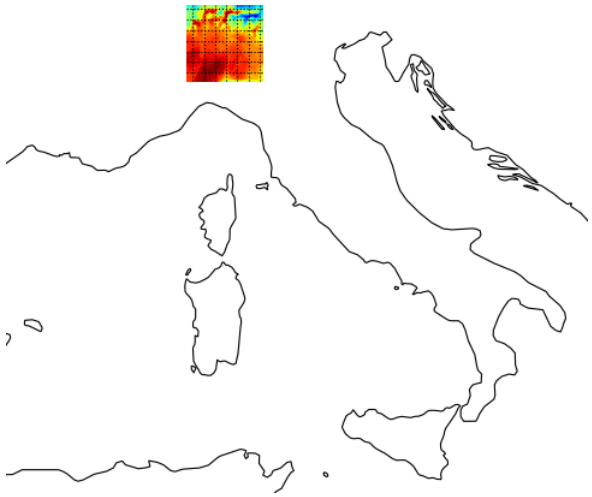

Figure 3: Regional NWP model

2.2 WRF Model

The development of WRF is a multi-agency effort to build a next-generation mesoscale forecast model and data assimilation system to advance the understanding and prediction of mesoscale weather and accelerate the transfer of research advances into operations [20].

WRF is a state-of-the-art atmospheric modeling system designed for both meteorological research and numerical weather prediction. This model allows to simulate several physical variables governing the state of the atmosphere on spatial and temporal resolutions sufficiently fine to allow their conversion into exploitable propagation data. Data such as temperature, pressure, humidity and wind profiles are downloaded across all pixels in space to cover the output grids of WRF. For each pixel, several tens of parameters are calculated. Among these, some will have a particular interest for the post-processing stage managed by this work.

The necessary steps to obtain an accurate NWP model are based on a set of Partial Differential Equations (PDEs) which describe the movement of moist air. These primitive equations are taken from principles of fluid mechanics. The Navier-Stokes equations that describe the atmosphere are nonlinear equations, therefore in physics in some cases they are called chaotic. This means that the dynamic system of the atmosphere has an exponential sensitivity to small variations in the initial conditions. Therefore a small uncertainty in the initial conditions means that the system can evolve in a completely unpredictable way over time. Two simulations with small uncertainties about the initial conditions can evolve completely differently and obtain completely different results over time.

In this work the WRF-1.5km Open Loop model is used and was provided by the CIMA research foundation [21]. The WRF-1.5km Open Loop configuration (without data assimilation) has 3 domains respectively having spatial resolution 13.5, 4.5 and 1.5 km with 50 vertical levels. The analysis and boundary data (hourly frequency) data are obtained from the Global Center for Global Practices System (GFS) model at 0.25 degrees of resolution. One run per day (00 UTC) is made with the GFS data with a forecast time horizon of 48 hours to have 2 full days of forecasting. This forecast is performed on computing resources at CINECA and is delivered to ARPAL within 730UTC.

2.2.1 Vertical Coordinate System

In the vertical direction, most NWP models use a pressure based coordinate system. The coordinate is therefore terrain-following near the ground and tends towards fixed pressure levels only near the top of the atmosphere, as seen in figure 4. The 50 levels are not equally spaced, in fact they correspond to equal pressure levels - not altitude - starting from the ground (following the terrain shape) and rising up to about 20 km altitude. An important point to make clear is that, because the vertical coordinates are based on pressure, which is a function of the time and space, a fixed value coordinate does not correspond to a fixed altitude.

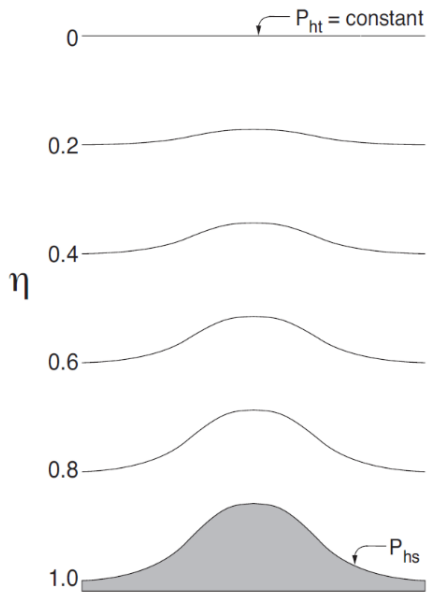

Figure 4: Pressure based vertical coordinates

2.2.2 Horizontal Coordinate System

The horizontal space covered by the data is approximately 162km by 162km square area over northern Italy, mapped by a Mercator grid.

Spatial resolution of data 50 x 108 x 108 with temporal resolution of 1 minute.

In terms of disk space, a month of simulation requires a storage capacity of around 700GB, for a year's worth of data that translates to 8.4TB.

2.2.3 Output Variables

The WRF variables relevant to the computation of propagation impairments are given in table 1. Most of these variables are 3D variables, i.e. in volume, and have dimensions (nz, ny, nz) at any given time step. There are also some surface variables of dimensions (ny, nx) which have a particularly notable interest for propagation such as the accumulated rain. The model produces Netcdf output files containing all the meteorological variables. The variables dependency and dimensions are stored in the header of the output file.

Table 1: WRF parameters

Variable	Description	Units
PH+PHB	Geopotential	m^2/s
T+300	Potential temperature	K
P+PB	Pressure	Pa
QVAPOUR	Vapour mixing ratio	kg/kg
QCLOUD	Cloud mixing ratio	kg/kg
QRAIN	Rain mixing ratio	kg/kg
RAINC	Convective rain	mm
RAINNC	Non-convective rain	mm
XLAT	Latitude	$°E$
XLONG	Longitude	$°N$

The geopotential $\varphi_g[m^2/s]$ serves as the reference spatial vertical coordinate. It is converted to the geopotential height $h[m]$ with:

$$h = \frac{\varphi_g}{g_0} \tag{1}$$

where $g_0 = 9.81 m^2 s^{-1}$ is standard Earth Gravity. The geopotential height h is roughly equivalent to the altitude above mean sea level.

In order to express the thermodynamic state of the atmosphere in a convenient form for the need of propagation calculations, one has to obtain the temperature $T[K]$ from the potential temperature $\theta[K]$ and total barometric pressure $p[Pa]$ with:

$$T = \theta \left(\frac{p}{10^5} \right)^{\frac{R}{c_p}} \tag{2}$$

where $R = 8.314 JK^{-1}mol^{-1}$ is the ideal gas constant and $c_p = 29.07 JK^{-1}mol^{-1}$ is the isobaric specific heat capacity for dry air at sea level and 0°C.

The water vapour partial pressure $p_{vap}[Pa]$ is calculated starting from the total barometric pressure p and the water vapour mass mixing ratio $QVAPOR$ according to Dalton's law:

$$p_{vap} = p \frac{QVAPOUR}{QVAPOUR + \frac{R_{air}}{R_{water}}} \tag{3}$$

where $R_{air} = 287.057 JK^{-1}kg^{-1}$ and $R_{water} = 461.52 JK^{-1}kg^{-1}$. The water vapour density $\rho_{vap}[g/m^3]$ is derived as:

$$\rho_{vap} = \frac{p_{vap}}{R_{water} T} \times 10^3 \tag{4}$$

To obtain the densities of liquid water, it is first necessary to compute the dry air density $\rho_{air}[g/m^3]$

$$\rho_{air} = \frac{p}{R_{air} T} \times 10^3 \tag{5}$$

then the density of cloud liquid water $M_c[g/m^3]$ and the density of rain water $M_r[g/m^3]$ are obtained as

$$M_c = QCLOUD \cdot \rho_{air} \tag{6}$$

$$M_r = QRAIN \cdot \rho_{air} \tag{7}$$

The rain rate calculation can be done by using the accumulated rain rate at time t and at one output time interval Δt before. The contribution from the convective and non-convective rain must also be accounted for such that

$$R_{rain_c}(t) = \frac{\int_0^t R_{rain_c} dt - \int_0^{t-\Delta t} R_{rain_c} dt}{\Delta t} = \frac{\int_{t-\Delta t}^t R_{rain_c} dt}{\Delta t} \tag{8}$$

$$R_{rain_{nc}}(t) = \frac{\int_0^t R_{rain_{nc}} dt - \int_0^{t-\Delta t} R_{rain_{nc}} dt}{\Delta t} = \frac{\int_{t-\Delta t}^t R_{rain_{nc}} dt}{\Delta t} \tag{9}$$

$$R_{rain}(t) = R_{rain_c}(t) + R_{rain_{nc}}(t) \tag{10}$$

In this work Δt is of 1 minute.

2.2.4 Remarks on WRF

This section summarizes some key points on the use of WRF outputs to estimate the impact of the troposphere on Earth-space links:

- the geopotential height h in is needed to convert the variables on a NWP grid to a grid suitable for the spatial integration of the propagation impairments, and for the slant path calculation.
- the XLAT and XLONG are used for the transformation of grid coordinate.
- the temperature T intervenes in all the specific attenuation models.
- the water vapour partial pressure p_{vap} and the water vapour density ρ_{vap} are needed for the water vapour specific attenuation, for the line-by-line method.
- the cloud liquid water density M_c is used for the cloud specific attenuation.
- the rain liquid water density M_r is used for the rain specific attenuation.
- the rain rate $R_{rain}(t)$ is used for the alternative rain specific attenuation model.

2.3 Alphasat and the Spino d'Adda Ground Station

The Alphasat commercial satellite operated by Inmarsat hosts Technological Demonstration Payloads (TDPs). The Italian Space Agency (ASI) successfully proposed the TDP#5, after renamed "Aldo Paraboni" Payload, in memory of the late professor of Politecnico di Milano, who greatly contributed to its conception and realization. The objective of the Aldo Paraboni payload is to perform a satellite communication experiment (named COMEX) and a propagation experiment (referred to as SCIEX, scientific experiment), as a part of the wider TRANSPONDERS program. The propagation experiment, which was supported by ASI and implemented by ESA, allows a better characterization of the atmospheric propagation channel at Ka band and Q band, making use of 2 coherent continuous-wave beacons operating at 19.701 and 39.402 GHz, respectively.

The main objective of the experiment is the investigation of first-order and second-order statistics of attenuation, joint depolarization and attenuation measurements, sky noise temperature, and instantaneous frequency scaling. Alphasat was successfully launched on 25 July 2013, from Kourou (French Guiana). The geosynchronous orbit is inclined on the equatorial plane; the orbit inclination is drifting from 0° to a maximum of 3°, before being reset to 0°. The satellite longitude is 25° East. The in orbit test campaign ended in December 2013, and the experimental campaign started at the end of February 2014.

Figure 5: The ASI Alphasat ground station located in Spino d'Adda

Three ground stations installed in Italy are currently collecting the Alphasat beacon signals: the 2 ASI main ground stations in Tito Scalo (Southern Italy) and Spino d'Adda (Northern Italy), respectively, and the La Sapienza-FUB station in Roma (Central Italy). This work contains data collected at Spino d'Adda pictured in figure 5. The station measures the copolar beacon signals at 19.701 and 39.402 GHz, with the 4.2-m-diameter antenna at an elevation angle of 35.5°. The coherent receiver acquires signal amplitude and phase with 16 Hz sampling rate, allowing a complete characterization of fast fluctuations because of tropospheric turbulence [16].

The radiometry data contains variables found in table 2.

Table 2: Variable list from Radiometry files

Variable	Description
datestring	string with date of recorded data
timeR	time vector UTC in seconds from 00:00:00 of the day
freqR	radiometric frequencies (GHz) for each hour of the day
BRTR	values of brightness temperatures (K)
RFR	rain flag (0: no rain; 1: rain)
AzR	Azimuth angle of the radiometer (deg)
ElR	elevation angle of the radiometer (deg)
Aest	matrix with the estimated attenuation (dB) for each fEX
fEX	frequencies of the Alphasat Aldo Paraboni experiment

An RpG-HATPRO profiler radiometer is installed at the station. The profiler is equipped with a heavy-duty dew blower system to prevent formation of dew and accumulation of raindrops on the antenna radome (in combination with a hydrophobic coating). Moreover, the dew blower heater system prevents

the formation of liquid water on the radome in foggy conditions (100% relative humidity). The absolute calibration is maintained by exploiting the hot internal black body target (routine calibration) and by using an external cold target (liquid nitrogen; this kind of calibration needed only after transportation of the instrument and every 6 months). A tipping bucket rain gauge and an ancillary meteorological station complete the equipment. The recorded weather data is reported in table 3.

Table 3: Variable list from meteorological files

Variable	Description
datestring	string with date of recorded data
timeM	time vector UTC in seconds from 00:00:00 of the day
PM	atmospheric pressure (hPa)
TM	ground temperature (°C)
HM	relative humidity (%a)
RA	rain amount (mm)
RR	rain intensity (mm/h)
GSH	GS Health (1: true; 0: other)

By combing these variables we can plot weather events and relate them to the attenuation of the signal, as seen in figure 6.

Figure 6: A flagged rain event with its rain rate and attenuation

To convert the received power levels (dBm) into total atmospheric attenua-

tion (dB) an estimation of the reference attenuation level by using radiometer data is needed [15]. The slant path atmospheric attenuation $A_{ref}(f, \vartheta)$ in dB, at frequency f and slant path elevation angle ϑ, is calculated during clear-sky periods, from the corresponding slant path brightness temperature, $T_B(K)$:

$$A_{ref}(f, \vartheta) = 10 \cdot \log \left(\frac{T_{mr}(f, \vartheta) - T_c}{T_{mr}(f, \vartheta) - T_{B(f,\vartheta)}} \right) \tag{11}$$

where $T_{mr}(K)$ is the monthly mean radiative temperature, calculated by applying the Liebe's mass absorption model to a large data set of local vertical atmospheric profiles, and $T_c(K)$ is the cosmic background temperature, typically 2.73 K at microwaves.

The tropospheric attenuation, $A_{rad}(f, \vartheta)$, at the beacon frequencies f = 19.701 GHz and f = 39.402 GHz, respectively, is estimated, in the absence of rain, as the linear combination of $A_{ref}(f, \theta)$, calculated at the 5 radiometric frequencies of 23.84, 27.84, 31.40, 51.26, and 52.28 GHz; $A_{rad}(f, \vartheta)$ is thus given by:

$$A_{rad}(f, \vartheta) = a_0 + \sum_{i=1}^{5} a_i A_{ref}(f_i, \vartheta) \tag{12}$$

where, as for $T_{mr}(f, \vartheta)$, the coefficients a_0 and a_i are calculated by regression of $A_{ref}(f, \theta)$ and $A_{rad}(f_i, \vartheta)$, which are calculated by applying cloud detection and mass absorption models to the local vertical profiles. The beacon power level time series, P_{beac} (dBm), are converted in total attenuation time series, $A_{tot,beac}$, through:

$$A_{tot,beac}(f, \vartheta) = -P_{beac}(f, \vartheta) + P_{beac,s}(f, \vartheta) + A_{rad}(f, \vartheta) \tag{13}$$

where $P_{beac,s}$ (dBm) is the beacon power level during clear sky periods and concurrent to A_{rad}.

Figure 7 shows estimated attenuation at frequencies f = 37.9 GHz and f= 48.1 GHz. The radiometer is sensitive only to absorption and not to scattering from hydrometeors during precipitation (as well as to scattering from turbulent eddies), A_{ref} can be calculated, through Equation 11, only during clear sky periods. For this reason we rely on the brightness temperature at f_1 = 23.84 and f_2 = 31.4 GHz, has been applied to preliminarily identify the presence of rain along the path. The sky status indicator (SSI) is calculated from 1-minute averaged brightness temperature data as:

$$SSI = \frac{T_B(f_2, \vartheta) - 10.3}{T_B(f_2, \vartheta)} \tag{14}$$

the SSI signal is thresholded by a robust hysteresis method with lower and upper thresholds equal to 0.73 and 0.87, respectively. Rain is present in the time intervals where the SSI signal exceeds the lower threshold and, at the same time, at least 1 SSI sample is above the upper threshold. The above thresholds have been chosen by comparing the cumulative distribution functions of rain rate

and SSI at given probability levels. This simple automatic procedure detects almost all rain events. However, it is not able to single out with high accuracy when precipitation begins and ends. Hence, the start and end time of each event have been subsequently adjusted by visual inspection of the rain rate time series derived from the rain gauge and of the received beacon signals.

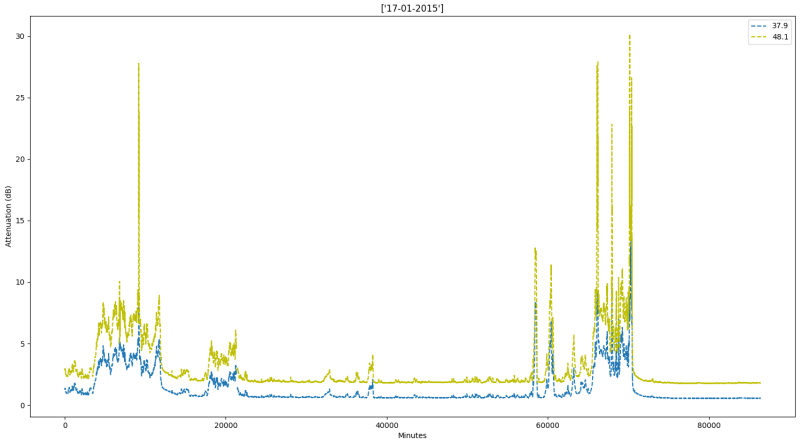

Figure 7: Estimated attenuation at frequencies $f = 37.9$ GHz and $f = 48.1$ GHz

3 Electromagnetic Wave Propagation through the Atmosphere

3.1 Fundamentals of Wave Propagation

An electromagnetic wave is characterized by variations of electric and magnetic fields. The oscillating motion of the field variations vibrating at a particular point in space at a given frequency excites similar vibrations at neighboring points, this is said to propagate. The separation in space of two consecutive oscillations is the wave length. Frequency f and wave length λ in free space are related by the equation $\lambda = c/f$,with c the speed of light. The power density, that is the watts per square meter of a propagating signal is inversely proportional to the distance from the source, this free space attenuation between two points at a distance of d can be written as:

$$L_a = 20 \log \left(\frac{4\pi d}{\lambda} \right) \tag{15}$$

Free-space loss L_a is measured in decibels and is present for all radio waves propagating in free space or in regions of space whose characteristics approximate the uniformity of free space, such as the earth's atmosphere. The frequency of the radio wave is an important factor when determining if other impairments will be introduced in addition to free space attenuation. As a general rule the higher the frequency (so the shorter the wavelength) the less the atmosphere can be approximated as free space, that is to mean there are other elements that interact with the propagating signal and therefore reducing its power density. The table 4 shows how frequency ranges are defined by the ITU standardization body.

Table 4: Frequency bands as defined by the ITU

Radar nomenclature		ITU nomenclature			
Radar letter designation	**Frequency range**	**Frequency range**	**Band No.**	**Adjectival band designation**	**Corresponding metric designation**
HF	3 MHz to 30 MHz	3 MHz to 30 MHz	7	High frequency (HF)	Decametric waves
VHF	30 MHz to 300 MHz	30 MHz to 300 MHz	8	Very high frequency (VHF)	Metric waves
UHF	300 MHz to 1000 MHz	0.3 GHz to 3 GHz	9	Ultra high frequency (UHF)	Decimetric waves
L	1 GHz to 2 GHz				
S	2 GHz to 4 GHz				
		3 GHz to 30 GHz	10	Super high frequency (SHF)	Centimetric waves
C	4 GHz to 8 GHz				
X	8 GHz to 12 GHz				
K_u	12 GHz to 18 GHz				
K	18 GHz to 27 GHz	30 GHz to 300 GHz	11	Extremely high frequency (EHF)	Millimetric waves
K_a	27 GHz to 40 GHz				
V	40 GZ to 75 GHz				
W	75 GHz to 110 GHz				
mm	110 GHz to 300 GHz	300 GHz to 3000 GHz	12	None	Decimillimetric

A signal will propagate from Earth's to beyond the atmosphere provided its frequency is high enough to traverse the ionosphere, which is roughly from

about 50km from the surface to 700 km above Earth. For frequencies below 20 MHz the ionosphere acts as a reflector or absorber, blocking the signal at different layers. Above 3GHz the ionosphere is essentially transparent, and at these frequencies the effects of the troposphere become the limiting factor [11].

Attenuation can be defined as the removal of power from a propagating signal traversing a medium and its effects can be seen in figure 8 It can be caused by two different physical effects: scattering and absorption.

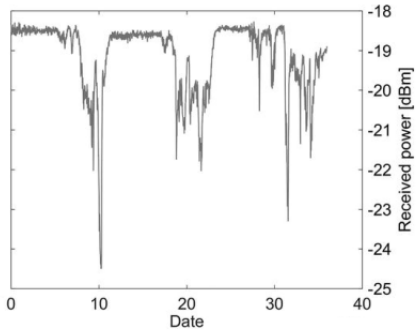

Figure 8: Attenuation events of a signal

Scattering

Scattering occurs when a wave interacts with a body and its energy is first absorbed and then re-emitted in multiple directions with different intensities. An example of basic scattering is the sun light through a thin cover of clouds. Instead of hitting the surface of the earth directly, the sun's light is weakened. This is because as the sun shines through the clouds, its light is scattered and only some of it ends up on the surface of the earth. In the context of this investigation some assumptions about the nature of scattering are made in order to make the atmospheric signal attenuation problem feasible:

- *Frequency coherent scattering:* The scattered signal maintains the same frequency as the incident wave.
- *Independent scattering:* There is no electromagnetic interaction between two separate particles. In the case of atmospheric conditions this assumption is valid and explained in detail in [18] which states that particles whose distance is more than three times their radius may be considered as independent.

The effects of multiple scattering will be neglected, which means a scattered wave is not scattered subsequently by another particle. If the scattering medium is composed of N similar particles, each of which scatters a quantity of energy e_s the total scattered energy can be written as $E_s = N * e_s$.

These assumptions give us the possibility to study the problem of attenuation starting from the attenuation due to a single particle, and then by integrating all contributions from the population to find the total attenuation of the medium.

Absorption

Absorption happens when the energy is converted into another form (for example heat) and therefore not re-emitted in the same form as the source.

For the purpose of designing satellite communication systems the concern regards the total attenuation of the the signal, not the specific kind of loss.

We are able to write the loss in energy as a function of the distance d in the attenuating medium as:

$$P_{loss} = -k_n P d \tag{16}$$

where k_n is the amount of power attenuated expressed in Neper per unit length.

By placing $P = P_0$ at $d = d_0$ and integrating over the total distance:

$$\ln \frac{P}{P_0} = -\int_0^d k_l dd \tag{17}$$

and the total attenuation A on the path is expressed in decibels as:

$$A = 10 \log \frac{P}{P_0} = \frac{10}{\ln 10} \ln \frac{P}{P_0} = -4.434 \int_0^d k_l \, \mathrm{d}d = -\int_0^d \gamma_a \, \mathrm{d}d \tag{18}$$

The attenuation coefficient γ_a describes the extent to which the radiant flux of a signal is reduced as it passes through a specific material, so it represents the attenuated power per unit length. It is therefore a key parameter to be calculated by the model.

When multiple factors contribute to the attenuation, just like the atmosphere, the attenuation coefficients can be summed and integrated along the path.

Refraction

Refraction of a propagating wave is a deflection that occurs when passing through the interface between one medium and another or through a medium of varying density. In a homogeneous medium the phase velocity of a wave is described as $\nu = (\epsilon\mu)^{-1/2}$. In free space this value is exactly the speed of light and is therefore given by $\nu = c = (\epsilon\mu)^{-1/2} = 3 * 10^8 ms^{-1}$ =constant.

3.2 Electromagnetic Properties of the Atmosphere

Electromagnetic waves interact with the constituents of the atmosphere principally as a function of their frequencies, and as a function of thermodynamic state (pressure and temperature) and the presence of water (humidity, hydrometeors). The atmosphere can be modeled as a stratified medium with variable refractive index. As the atmosphere is composed of layers, each with a varying

refractive index, the signal can be subject to several degrees of deviation. This phenomena can be used for certain applications, for instance to reach receivers beyond the horizon of the Earth, bouncing the signal off a specific layer of the atmosphere.

In the atmosphere, while the value of the relative magnetic permeability $\mu_r = \mu/\mu_0$ can be approximated as constant and equal to one, the relative dielectric permittivity $\epsilon_r = \epsilon/\epsilon_0$varies with frequency, and with atmospheric conditions such as temperature, pressure and humidity, resulting in a variation of phase velocity of the propagating signal. The refractive index n, which is the ratio of velocity of the wave in free space and its phase velocity in the medium in which it is propagating, is the square root of the relative dielectric permittivity:

$$n = \frac{c}{\nu} = \epsilon_r^{1/2} \tag{19}$$

For media that both deviate and attenuate a wave, the refractive index is written in complex form as:

$$m = n - ik \tag{20}$$

where both components are dependent on the frequency, and k is associated to the losses due to absorption. In a perfect dielectric material $k = 0$.

The effects on propagation due to the nature of the atmosphere can be split into ionospheric and troposheric factors. The ionosphere is a layer of the atmosphere with a high concentration of electrons and electrically charged atoms and molecules. Ionospheric effects regard the rotation of polarization of the wave, due to the electromagnetic interaction between the wave and the ionized medium, or due to the small-scale irregularities in the structure of the atmosphere which cause rapid fluctuations in the phase and amplitude of the propagated signal. Above 3 GHz these effects become irrelevant.

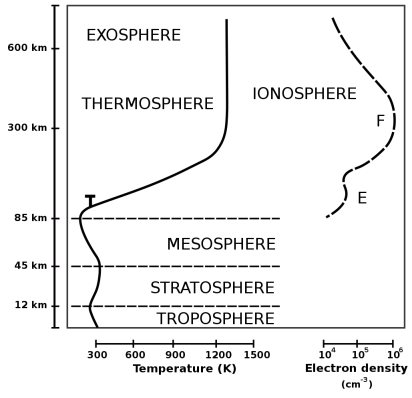

Figure 9: Atmospheric layers

The troposphere can be considered as the area where all meteorological phenomena take place. This layer of the atmosphere is made up of gases and hydrometeors, which degrade the signal to different degrees. Composed by a mixture of different gases (78.08% nitrogen, 20.95% oxygen, 0.93% argon, 0.04% carbon dioxide, and small amount of other gases), it contains 75% of the atmosphere's mass and 99% of the total mass of water vapour and aerosols [14]. For frequencies in the SHF range (3-30 GHz), which are largely used in satellite communications, this layer is of critical importance.

Precipitation, hail, ice crystals and clouds along the transmission path have a degrading effect and is particularly damaging for signals. Impairment strongly affects the prescribed quality of service to be delivered by satellite operators. Table 5 summarizes the effects of the atmosphere on radio signals:

Table 5: Attenuation types

Attenuation Type	Cause
Absorption	Atmospheric gases
Scattering & Absorption	Hydrometeors (rain, hail, snow, cloud)
Depolarization	Hydrometeors and multipath
Noise Emission	All atmospheric constituents
Scintillation (rapid variations)	Turbulence or refractive index irregularities
Angle of arrival variations	Small scale fluctuations in refractive index
Bandwidth limitations	Multipath and dispersive properties
Antenna gain degradations	phase decorrelation across aperture

Power losses coming from hydrometeor scattering/absorption represent an important part of the total impairment effects on signal atmospheric propagation, due to tropospheric phenomena like cloud formation, rain, snow and ice.

3.2.1 Attenuation Caused by Atmospheric Gases

The gaseous elements of the Earth's atmosphere which can interact with electromagnetic waves at the frequencies of interest (1-1000 GHz) are limited to oxygen and water vapour. The first 3 absorption bands are centered at 22GHz (H2O), 60GHz (O2) and 118.8 GHz(O2) and are shown in figure 10.

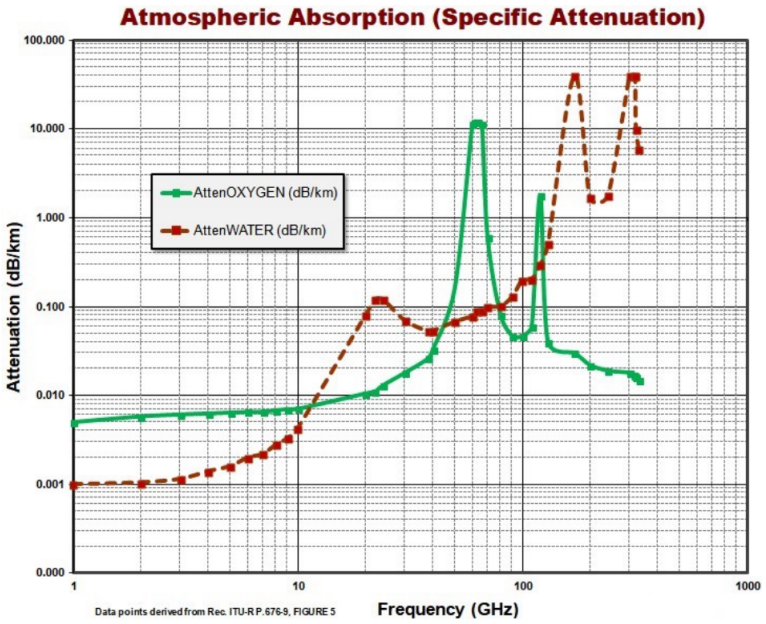

Figure 10: Water vapour and Oxygen absorption bands

The permanent magnetic moment of the oxygen molecule interacts with the magnetic field of the radio wave, while the water vapour molecule electric dipole interacts with the electric field of the wave, producing a quantum level change in the rotational energy of the molecule, which absorbs energy.

The modeling of this gaseous attenuation is achieved as a summation over all the absorption lines relevant to radio-waves. The specific attenuation at frequencies up to 1000 GHz can be accurately evaluated at all values of pressure, temperature and humidity as summation of the spectral lines from oxygen and water vapour, with small additional values for the non-resonant Debye spectrum of oxygen below 10 GHz, a pressure-induced nitrogen attenuation above 100 GHz and a wet continuum to account for the excess water vapour-absorption found experimentally [12].

The atmospheric values of interest are:

- p: dry air pressure, in hPa
- e: water vapour partial pressure, also in hPa
- p_{tot}: total barometric pressure $p_{tot} = p + e$
- $\theta = \frac{300}{T}$
- T: Temperature, given in Kelvin

The specific gaseous attenuation is given by:

$$\gamma = \gamma_o + \gamma_w = 0.1820\, f \left(N''_{Oxygen}(f) + N''_{WaterVapour}(f) \right) \tag{21}$$

where γ_o and γ_w are the specific attenuation (dB/km) due to dry air (oxygen, pressure-induced nitrogen and non-resonant Debye attenuation) and water vapour, respectively, f is the frequency (GHz), and $N''_{Oxygen}(f)$ (f and $N''_{WaterVapour}(f)$are the imaginary parts of the frequency-dependent complex refractivities:

$$N''_{Oxygen}(f) = \sum_{i(Oxygen)} S_i F_i + N''_D(f) \tag{22}$$

$$N''_{WaterVapour}(f) = \sum_{i(WaterVapour)} S_i F_i \tag{23}$$

S_i is the strength of the i-th oxygen or water vapour line, F_i is the oxygen or water vapour line shape factor. The summations are evaluated over the spectral lines in the spectroscopic data tables: table 6 is for oxygen and table 7 is for water vapour.

$N''_D(f)$ is the dry continuum due to pressure-induced nitrogen absorption and the Debye spectrum. The line strength is given by:

$$S_{i_{ox}} = a_1 10^{-7} p \theta^3 \exp\left[a_2 (1-\theta)\right] \tag{24}$$

$$S_{i_{wv}} = b_1 10^{-1} e \theta^{3.5} \exp\left[b_2 (1-\theta)\right] \tag{25}$$

the line shape factor for oxygen is given by:

$$F_{i_{ox}} = \frac{f}{f_{i_{ox}}} \left[\frac{\Delta f_{ox} - \delta (f_{i_{ox}} - f)}{(f_{i_{ox}} - f)^2 + (\Delta f_{ox})^2} + \frac{\Delta f_{ox} - \delta (f_{i_{ox}} + f)}{(f_{i_{ox}} + f)^2 + (\Delta f_{ox})^2} \right] \tag{26}$$

where delta is a correction factor that arises from interference effects in oxygen lines:

$$\delta = (a_5 + a_6 \Theta) \times 10^{-4} (p+e) \theta^{0.8} \tag{27}$$

while the line shape factor for water vapour is given by:

$$F_{i_{wv}} = \frac{f}{f_{i_{wv}}} \left[\frac{\Delta f_{wv}}{(f_{i_{wv}} - f)^2 + (\Delta f_{wv})^2} + \frac{\Delta f_{wv}}{(f_{i_{wv}} + f)^2 + (\Delta f_{wv})^2} \right] \tag{28}$$

where $f_i$is the oxygen and water vapour line frequency and Δf_{wv} is the width of line given by:

$$\Delta f_{ox} = a_3 \times 10^{-4} \left(p \theta^{(0.8 - a_4)} + 1.1 e \theta \right) \tag{29}$$

$$\Delta f_{wv} = b_3 \times 10^{-4} \left(p\theta^{b_4} + b_5 e\theta^{b_6} \right) \tag{30}$$

the line width Δf_{wv} is modified to account for Zeeman splitting of oxygen lines and Doppler broadening of water vapour lines:

$$\Delta f_{ox} = \sqrt{\Delta f_{ox}^2 + 2.25 \times 10^{-6}} \tag{31}$$

$$\Delta f_{wv} = 0.535 \Delta f_{wv} + \sqrt{0.217 \Delta f_{wv}^2 + \frac{2.1316 \times 10^{-12} f_{i_{wv}}}{\theta}} \tag{32}$$

the dry air continuum arises from the non-resonant Debye spectrum of oxygen below 10 GHz and a pressure-induced nitrogen attenuation above 100 GHz.

$$N(f)_D'' = fp\theta^2 \left[\frac{6.14 \times 10^{-5}}{d\left[1 + \left(\frac{f}{d}\right)^2\right]} + \frac{1.4 \times 10^{-12} p\theta^{1.5}}{1 + 1.9 \times 10^{-5} f^{1.5}} \right] \tag{33}$$

where $d$is the width parameter for the Debye spectrum:

$$d = 5.6 \times 10^{-4} (p + e) \theta^{0.8} \tag{34}$$

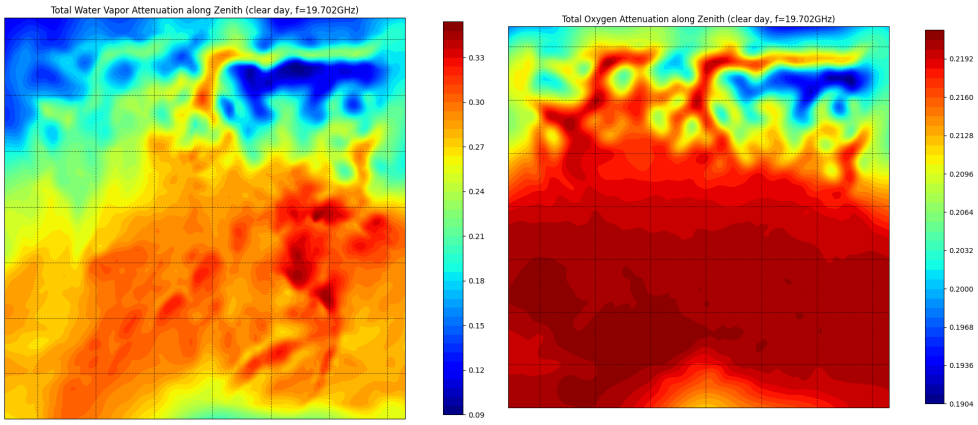

Figure 11: Zenithal Water vapour and Oxygen Attenuation, f=19.702GHz

Table 6: Spectroscopic data for Oxygen attenuation

$f_{i_{ox}}$	a_1	a_2	a_3	a_4	a_5	a_66
50.474214	0.975	9.651	6.690	0.0	2.566	6.850
50.987745	2.529	8.653	7.170	0.0	2.246	6.800
51.503360	6.193	7.709	7.640	0.0	1.947	6.729
52.021429	14.320	6.819	8.110	0.0	1.667	6.640
52.542418	31.240	5.983	8.580	0.0	1.388	6.526
53.066934	64.290	5.201	9.060	0.0	1.349	6.206
53.595775	124.600	4.474	9.550	0.0	2.227	5.085
54.130025	227.300	3.800	9.960	0.0	3.170	3.750
54.671180	389.700	3.182	10.370	0.0	3.558	2.654
55.221384	627.100	2.618	10.890	0.0	2.560	2.952
55.783815	945.300	2.109	11.340	0.0	-1.172	6.135
56.264774	543.400	0.014	17.030	0.0	3.525	-0.978
56.363399	1331.800	1.654	11.890	0.0	-2.378	6.547
56.968211	1746.600	1.255	12.230	0.0	-3.545	6.451
57.612486	2120.100	0.910	12.620	0.0	-5.416	6.056
58.323877	2363.700	0.621	12.950	0.0	-1.932	0.436
58.446588	1442.100	0.083	14.910	0.0	6.768	-1.273
59.164204	2379.900	0.387	13.530	0.0	-6.561	2.309
59.590983	2090.700	0.207	14.080	0.0	6.957	-0.776
60.306056	2103.400	0.207	14.150	0.0	-6.395	0.699
60.434778	2438.000	0.386	13.390	0.0	6.342	-2.825
61.150562	2479.500	0.621	12.920	0.0	1.014	-0.584
61.800158	2275.900	0.910	12.630	0.0	5.014	-6.619
62.411220	1915.400	1.255	12.170	0.0	3.029	-6.759
62.486253	1503.000	0.083	15.130	0.0	-4.499	0.844
62.997984	1490.200	1.654	11.740	0.0	1.856	-6.675
63.568526	1078.000	2.108	11.340	0.0	0.658	-6.139
64.678910	461.300	3.181	10.380	0.0	-3.968	-2.590
65.224078	274.000	3.800	9.960	0.0	-3.528	-3.680
65.764779	153.000	4.473	9.550	0.0	-2.548	-5.002
66.302096	80.400	5.200	9.060	0.0	-1.660	-6.091
66.836834	39.800	5.982	8.580	0.0	-1.680	-6.393
67.369601	18.560	6.818	8.110	0.0	1.956	-6.475
67.900868	8.172	7.708	7.640	0.0	-2.216	-6.545
68.431006	3.397	8.652	7.170	0.0	-2.492	-6.600
68.960312	1.334	9.650	6.690	0.0	-2.773	-6.650
118.750334	940.300	0.010	16.640	0.0	-0.439	0.079
368.498246	67.4	0.048	16.4	0.0	0.0	0.0
424.76302	637.7	0.044	16.4	0.0	0.0	0.0
487.249273	237.4	0.049	16	0.0	0.0	0.0
715.392902	98.1	0.145	16	0.0	0.0	0.0
773.83949	572.3	0.141	16.2	0.0	0.0	0.0
834.145546	183.1	0.145	14.7	0.0	0.0	0.0

Table 7: Spectroscopic data for water vapour attenuation

$f_{i_{wv}}$	b_1	b_2	b_3	b_4	b_5	b_6
22.235080	0.1079	2.144	26.38	0.76	5.087	1.00
67.803960	0.0011	8.732	28.58	0.69	4.930	0.82
119.995940	0.0007	8.353	29.48	0.70	4.780	0.79
183.310087	2.273	0.668	29.06	0.77	5.022	0.85
321.225630	0.0470	6.179	24.04	0.67	4.398	0.54
325.152888	1.514	1.541	28.23	0.64	4.893	0.74
336.227764	0.0010	9.825	26.93	0.69	4.740	0.61
380.197353	11.67	1.048	28.11	0.54	5.063	0.89
390.134508	0.0045	7.347	21.52	0.63	4.810	0.55
437.346667	0.0632	5.048	18.45	0.60	4.230	0.48
439.150807	0.9098	3.595	20.07	0.63	4.483	0.52
443.018343	0.1920	5.048	15.55	0.60	5.083	0.50
448.001085	10.41	1.405	25.64	0.66	5.028	0.67
470.888999	0.3254	3.597	21.34	0.66	4.506	0.65
474.689092	1.260	2.379	23.20	0.65	4.804	0.64
488.490108	0.2529	2.852	25.86	0.69	5.201	0.72
503.568532	0.0372	6.731	16.12	0.61	3.980	0.43
504.482692	0.0124	6.731	16.12	0.61	4.010	0.45
547.676440	0.9785	0.158	26.00	0.70	4.500	1.00
552.020960	0.1840	0.158	26.00	0.70	4.500	1.00
556.935985	497.0	0.159	30.86	0.69	4.552	1.00
620.700807	5.015	2.391	24.38	0.71	4.856	0.68
645.766085	0.0067	8.633	18.00	0.60	4.000	0.50
658.005280	0.2732	7.816	32.10	0.69	4.140	1.00
752.033113	243.4	0.396	30.86	0.68	4.352	0.84
841.051732	0.0134	8.177	15.90	0.33	5.760	0.45
859.965698	0.1325	8.055	30.60	0.68	4.090	0.84
899.303175	0.0547	7.914	29.85	0.68	4.530	0.90
902.611085	0.0386	8.429	28.65	0.70	5.100	0.95
906.205957	0.1836	5.110	24.08	0.70	4.700	0.53
916.171582	8.400	1.441	26.73	0.70	5.150	0.78
923.112692	0.0079	10.293	29.00	0.70	5.000	0.80
970.315022	9.009	1.919	25.50	0.64	4.940	0.67
987.926764	134.6	0.257	29.85	0.68	4.550	0.90
1,780.000000	17506	0.952	196.3	2.00	24.15	5.00

3.2.2 Hydrometeors

Before being able to define the specific attenuation coefficient for other atmospheric effects, a detailed analysis into the properties of water droplets (hydrometeors) must be carried out.

Due to the random nature of tropospheric phenomena, the specific atten-

uation can be described through models which merge physical and stochastic approaches: first computing the physical attenuation properties of a single hydrometeor and then deriving the overall effect of an entire population of hydrometeors.

The attenuation properties of a single hydrometeor are modeled in 3 ways: Mie theory, the Rayleigh approximation and the T-Matrix model.

These models take as input the frequency of the signal, the refractive index of the medium and the scattering angle. Some assumptions must be made regarding the nature of the particles:

- *Particle dimension:* the physical size of the hydrometeors determines which model is most appropriate. The smaller the particle the less it interacts with longer wavelengths. Hydrometeors are larger than particles suspended in clouds. The size is defined in terms of equivalent diameter, which describes the diameter as a perfect sphere.

- *Particle shape:* the shape of the drop is strictly related to the dimension [10]. The smaller the dimension the closer to a sphere it is. A falling hydrometeor flattens due to the drag caused by the atmosphere, which interacts with the superficial tension of the drop. So, the larger the particle the more it takes the form of an oblate spheroid. This also limits the maximum size of a particle. Once a particle exceeds a certain dimension, usually around 4 mm, it breaks up into smaller particles. The parameter that describes the oblateness is refered to as the axis ratio. The shape of the particle in relation to size can be seen in figure 12

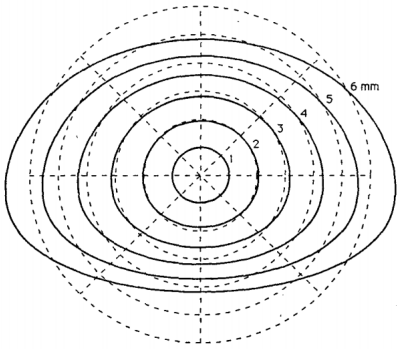

Figure 12: Water drop shape as modeled by Beard and Chuang

- *Particle orientation angle:* The orientation angle is defined as the tilt of the drop with respect to the incident wave. By fixing a reference system at the center of the drop, the orientation angle is defined by two Euler angles α and β and can be seen in figure 13. The relative change in shape and size due to the orientation angle will modify the dielectric properties. In

order reduce the complexity of this phenomenon a Gaussian distribution of particle orientation can be employed.

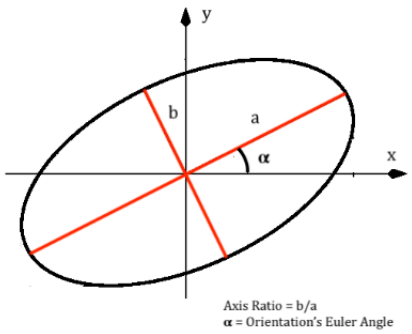

Figure 13: Particle orientation

- *Particle composition:* Hydrometeors can be considered homogeneous, composed of just water, making the calculation of the dielectric constant relatively simple, the computation of which takes into account only wavelength and temperature and is based on Deybe's theory [18].For snow, because of the simultaneous presence of air, water and ice the dielectric constant is evaluated empirically. It is possible to notice that water has a larger imaginary part of the dielectric constant, which is the part related to absorption, so ice absorbs less than rain.

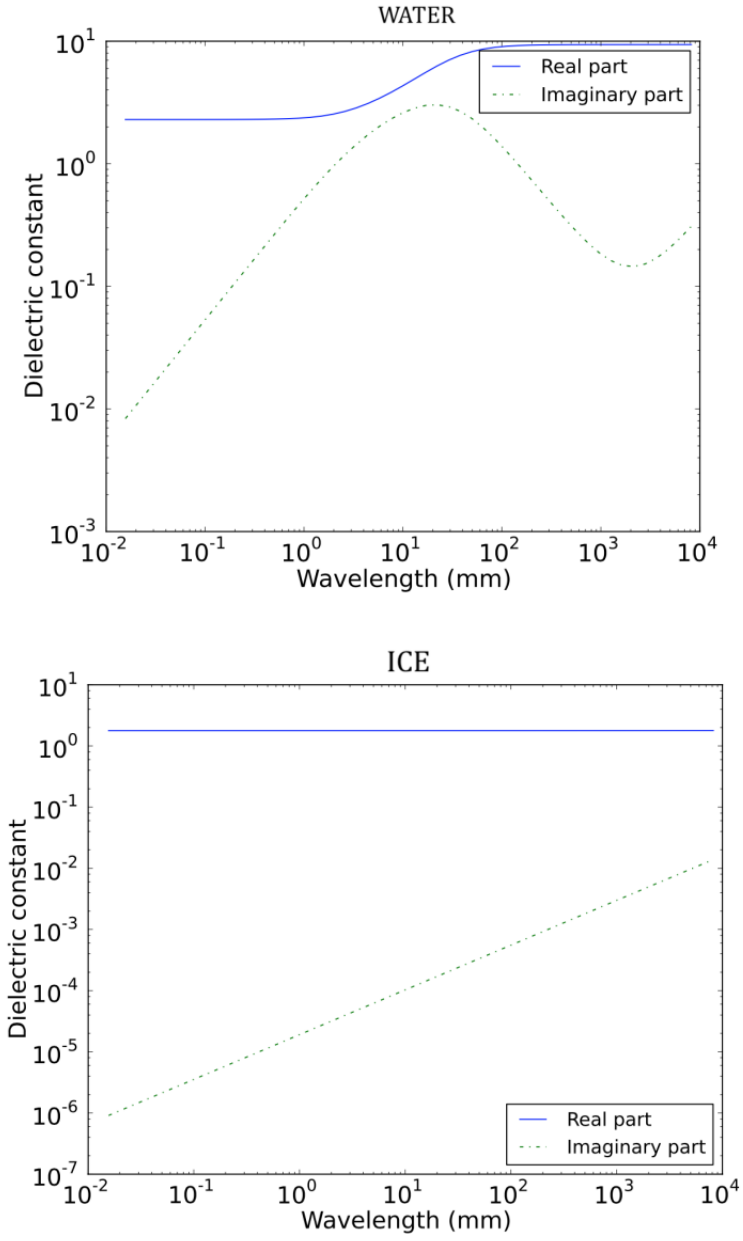

Figure 14: Dielectric permittivity of water and ice

The 3 models mentioned above all output a fundamental element for attenuation known as the attenuation cross section, which is the surface intercepting the amount of energy equal to that taken in total by the scatterer.

3.2.3 Mie Scattering Theory

Also known as the Mie solution to Maxwell's equations, Mie scattering theory describes the scattering of an electromagnetic plane wave by a homogeneous sphere immersed in a non-absorbing medium. It is an exact method which starts from the set of Maxwell's equations, the solution takes the form of an infinite series of spherical multipole partial waves [8].

As previously described, when the wave impinges on a body with dielectric properties which are different from the ones in the surrounding medium, the energy transported by the signal is partly absorbed and partly scattered in all directions, in the form of a field with the same wavelength as the exciting energy. Following van de Hulst[1981]:

$$\sigma_e = \frac{\lambda^2}{2\pi} \sum_{\nu=1}^{\infty} (2\nu + 1) \, \mathbb{R} \{a_\nu + b_\nu\} \tag{35}$$

a_ν and b_ν are Mie coefficients and are obtained through Bessel functions by inputting α and m. The index ν is the order of the induced electric b_ν and magnetic a_ν modes:

$$a_\nu = \frac{\psi'_\nu(y)\,\psi_\nu(x) - m\psi_\nu(y)\,\psi'_\nu(x)}{\psi'_\nu(y)\,\varsigma_\nu(x) - m\psi_\nu(y)\,\varsigma'_\nu(x)} \tag{36}$$

$$b_\nu = \frac{m\psi'_\nu(y)\,\psi'_\nu(x) - \psi_\nu(y)\,\psi'_\nu(x)}{m\psi'_\nu(y)\,\varsigma'_\nu(x) - \psi_\nu(y)\,\varsigma'_\nu(x)} \tag{37}$$

where $x = kr_d$, $y = mkr_d = mx$ are defined in function of the wave number and drop radius r_d,and where the Ricatti-Bessel functions ψ_ν, χ_ν and $\varsigma_\nu$are given by:

$$\psi_\nu(z) = z j_\nu(z) \tag{38}$$

$$\chi_\nu(z) = -z y_\nu(z) \tag{39}$$

$$\varsigma_\nu(z) = z h_\nu^{(2)} = \psi_\nu(z) + j\chi_\nu(z) \tag{40}$$

and are expressed as spherical Bessel functions $j_\nu$and $y_\nu$and of the spherical Hankel function $h_\nu^{(2)}$.

3.2.4 Rayleigh Scattering

Rayleigh Scattering is the scattering model for electromagnetic radiation by particles much smaller than the wavelength of the radiation. It is an approximated solution to the Mie theory. For us it is relevant because it is the starting point from which cloud attenuation can be calculated. The consequence of having particles of radius $r_d \leq 10^{-5}m$ is that the term $\nu = 1$ is dominant and the summation $\sum_{\nu=1}^{\infty}(2n+1)$ in the original Mie σ_e function can be expressed as a

function of r_d [?], this is clear in figure 15 moreover with the same conditions a_1 is much larger than b_1 (Table 16) from which a simplified σ_e function becomes:

$$\sigma_e \approx \frac{3\lambda^2}{2\pi}\mathbb{R}\{a_1\} = \frac{6}{x^2}\mathbb{R}\{a_1\} \times \pi r_d^2 \tag{41}$$

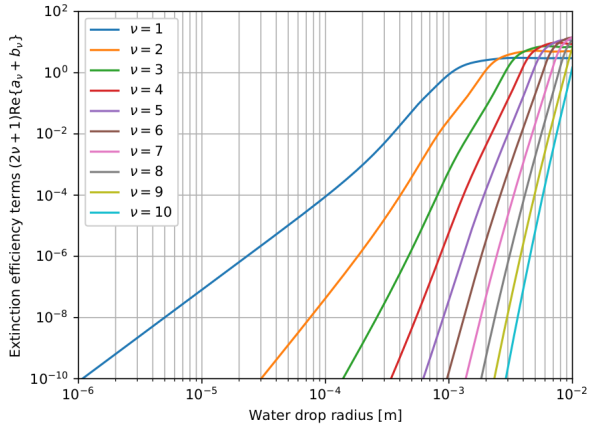

Figure 15: Extinction efficiency terms

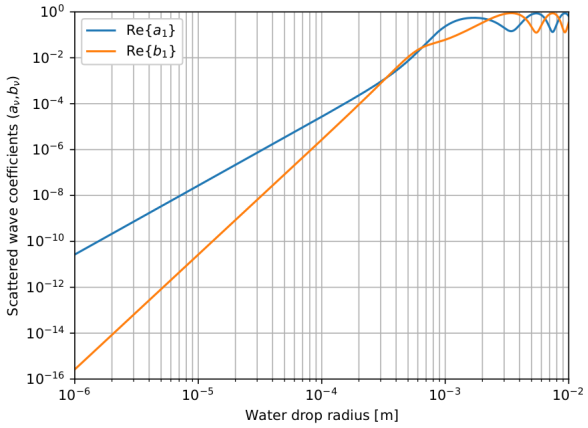

Figure 16: Scattered wave coefficients $a_1$and b_1

This function can be further simplified by working on a_1. The Ricatti-Bessel functions used in the Mie scattering model and Rayleigh formulas for spherical Bessel functions:

$$j_\nu(z) = \left(-\frac{d}{dz}\right)^\nu \left[\frac{\sin(z)}{z}\right] \tag{42}$$

$$y_\nu(z) = -\left(-\frac{d}{dz}\right)^\nu \left[\frac{\cos(z)}{z}\right] \tag{43}$$

with $z \to 0$, we have:

$$\psi_1(z) \approx \frac{1}{3}z^2 \tag{44}$$

$$\psi_1'(z) \approx \frac{2}{3}z^2 \tag{45}$$

$$\chi_1(z) \approx \frac{1}{z} \tag{46}$$

$$\chi_1'(z) \approx -\frac{1}{z^2} \tag{47}$$

where $x$in the definition of a_ν is very small for microwaves as $r_d \ll \lambda$ and this is true for y and for liquid water $|m| \lesssim 10$, so substituting these new values for ψ_ν and χ_ν in a_ν:

$$a_1 \approx j\frac{2x^3}{3}\frac{m^2-1}{m^2+2} \tag{48}$$

and by expanding it to obtain its real part it becomes:

$$a_1 = \frac{2x^3}{3}\frac{3\epsilon_r'' + j\left(\epsilon_r''^2 + (\epsilon_r'-1)(\epsilon_r'+2)\right)}{(\epsilon_r'+2)^2 + \epsilon_r''^2} \tag{49}$$

finally by re-arranging Mie's formula for extinction cross section:

$$\sigma_e = 24\pi^2\frac{r_d^3}{\lambda}\frac{1}{\epsilon_r''^2\left(\left(\frac{\epsilon_r'+2}{\epsilon_r''}\right)^2+1\right)} \tag{50}$$

In this way the extinction cross section depends only on the drop dimension r_d^3 , and if the mass of drop per unit volume is known (liquid water content) then it is not necessary to know the details of the size distribution.

3.2.5 T-Matrix Model

The T-matrix model stems from the idea of Peter C. Waterman in 1965. While Mie theory and Rayleigh's approximation are very good approximations for spherical particles, the T-matrix method allows for the calculation of the scattering wave caused by different shapes particles. By using a set of functions known as Spherical Vector Wave Functions (SWVF) and decomposing the incident and scattered electromagnetic fields, this models allows to go from incident to scattered waves by means of a Transition Matrix [22]. The scattered wave is defined by an integral equation which involves the induced electric and magnetic surface currents of the particle, which are described using Maxwell's equations.

The incident field and scattered fields can be expressed through the use of 2 SWVF M and N, along with two expansion coefficients a_{mn} and b_{mn} for the incident field and p_{mn} and q_{mn} for the scattered field respectively:

$$E_{inc}(R) = \sum_{n=1}^{n_{max}} \sum_{m=-n}^{n} \left[a_{mn} RM_{mn}(R) + b_{mn} RN_{mn}(R) \right] \tag{51}$$

$$E_{sca}(R) = \sum_{n=1}^{n_{max}} \sum_{m=-n}^{n} \left[p_{mn} M_{mn}(R) + q_{mn} N_{mn}(R) \right] \qquad with\,|R| > r_0 \tag{52}$$

r_0 is the radius of the sphere around the scattering particle, with the origin of the coordinate system in the center of the particle.

By taking advantage of the linearity of the Maxwell equations and the orthogonality property of the spherical functions, it is possible to integrate the particle's surface, giving a set of linear equations with unknowns, i.e. the expansion coefficients. Through a transition matrix the scattered field expansion coefficients can be placed in relationship with the incident field coefficients:

$$\begin{bmatrix} p \\ q \end{bmatrix} = T \begin{bmatrix} a \\ b \end{bmatrix} = \begin{bmatrix} T^{11} & T^{12} \\ T^{21} & T^{22} \end{bmatrix} \begin{bmatrix} a \\ b \end{bmatrix} \tag{53}$$

the expansion coefficients a_{mn} and b_{mn} of the incident field can be calculated using closed-form analytical expressions. Then matching the boundary conditions, and truncating the series at some finite value of spherical modal indices, also p_{mn} and q_{mn} can be derived, together with the surface currents and the scattered field, and so the T-Matrix elements. The elements of the matrix are independent of the incident and scattered fields and depend only on the shape, size parameter, refractive index of the scattering particle, and the on its orientation with respect to the reference frame. The extinction cross section is given by:

$$\sigma_e = -\frac{2\pi}{\lambda^2} \mathbb{R} \left(\sum_{n=1}^{n_{max}} \sum_{m=-n}^{n} \left[T_{mn}^{11} + T_{mn}^{12} \right] \right) \tag{54}$$

Several open-source libraries for the numerical computation of the T-Matrix are available. The model for rain attenuation used in this work makes use of the Python library "PyTMatrix" by Jussi Leinonen in 2014. The "Scatterer" module allows the computation of the T-Matrix for the defined particle, and takes as input:

- *radius*: the radius of the equivalent sphere;
- *wavelength*: the wavelength of the EM wave;
- *refractive index*: the complex refractive index of the scatterer;
- *axis ratio*: the horizontal-to-rotational axis ratio a/b;

Once everything is defined and the "Scatterer" is computed, through the module "ext_xsect" it is possible to evaluate the required cross section. An interesting feature of the "Scatterer" module is the possibility of orientation averaging: the orientation of the particle with respect to the reference frame, defined on the basis of the Euler angles α, β, and the orientation of the incident and scattered beam, thorough the Zenith and Azimuth angles ϑ, ψ. By setting an orientation probability distribution function, e.g. uniform PDF or Gaussian PDF.

3.3 Attenuation Caused by Clouds

In clouds, because water droplets are generally smaller than 0.01 cm in diameter, the main cause for attenuation is absorption, while scattering losses are secondary. Under these conditions Rayleigh's approximation is valid and thus the distribution of the water particles within the cloud can ignored. The key contributor to the cloud attenuation is the cloud's liquid water content.

The liquid water content M describes the mass of water drops in the volume units of the cloud. The liquid water content is therefore the measure of the mass of the water in a cloud in a specified amount of dry air. The liquid water content of a particular cloud varies significantly depending on the type of cloud in the atmosphere at a given location. The classification of the cloud is related to the liquid water content.

Clouds with low density M such as cirrus clouds contain a small amount of water, with values around $0.03 g/m^3$. Clouds with high densities, like cumulonimbus clouds have much higher liquid water content, with values around $1 \sim 3 g/m^3$. Table 8 shows the liquid water content of various cloud types.

Table 8: Liquid water content of various cloud types

Cloud Type	M
Cirrus	0.03
Fog	0.05
Stratus	0.25-0.30
Cumulus	0.25-0.30
Stratocumulus	0.45
Cumulonimbus	1.0-3.0

The specific cloud attenuation γ_c $[dB/km2]$ is a function of clouds' liquid water content M_c $[g/m3]$ and a coefficient K_C, which is a function of frequency and temperature. The specific attenuation within a cloud can be written as:

$$\gamma_c = K_c M_c \tag{55}$$

The value for K_c is calculated based on the Rayleigh scattering model previously mentioned, and uses a double Debye model to calculate the dielectric permittivity $\varepsilon(f)$ of water. The following procedure can be found in recommendation ITU-R Rec P. 840 [13].

$K_c$is in $[(db/km^2)/(g/m^3)]$ and is given by:

$$K_c = \frac{0.819f}{\varepsilon^{''}(1+\eta)} \tag{56}$$

where η is given by:

$$\eta = \frac{2+\varepsilon^{'}}{\varepsilon^{''}} \tag{57}$$

The complex dielectric permittivity of water is:

$$\varepsilon^{''}(f) = \frac{f(\varepsilon_0 - \varepsilon_1)}{f_p\left[1+\left(\frac{f}{f_p}\right)^2\right]} + \frac{f(\varepsilon_1 - \varepsilon_2)}{f_s\left[1+\left(\frac{f}{f_s}\right)^2\right]} \tag{58}$$

$$\varepsilon^{'}(f) = \frac{\varepsilon_0 - \varepsilon_1}{\left[1+\left(\frac{f}{f_p}\right)^2\right]} + \frac{\varepsilon_1 - \varepsilon_2}{\left[1+\left(\frac{f}{f_s}\right)^2\right]} + \varepsilon_2 \tag{59}$$

where:

$$\varepsilon_0 = 77.66 + 103.3(\theta - 1) \tag{60}$$

$$\varepsilon_1 = 0.0671\varepsilon_0 \tag{61}$$

$$\varepsilon_2 = 3.52 \tag{62}$$

and as previously stated $\theta = \frac{300}{T}$.

The principal relaxation frequency, f_p, and secondary relaxation frequency, f_s, both in GHz, are:

$$f_p = 20.20 - 146(\theta - 1) + 316(\theta - 1)^2 \tag{63}$$

$$f_s = 39.8f_p \tag{64}$$

With an increase in signal frequency the attenuation due to clouds increases [23]. And as the temperature of the clouds decreases, the attenuation value increases as seen in figure 17

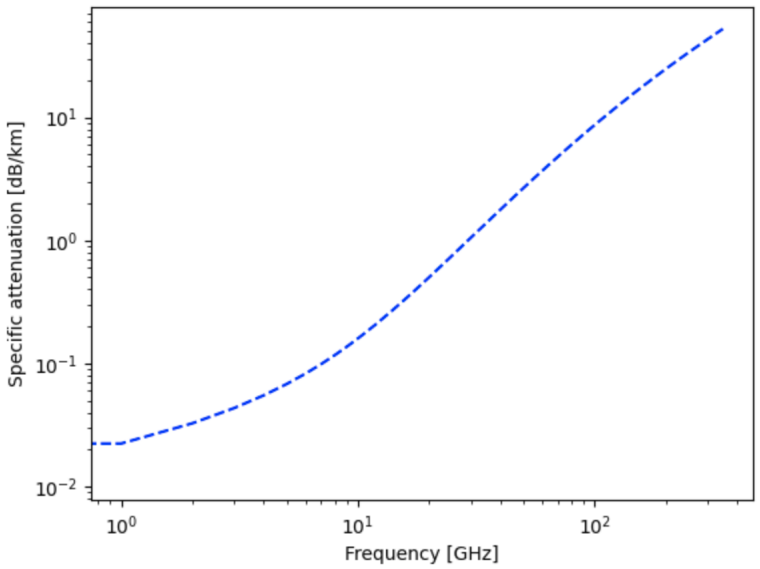

Figure 17: Cloud attenuation across 1-1000GHz

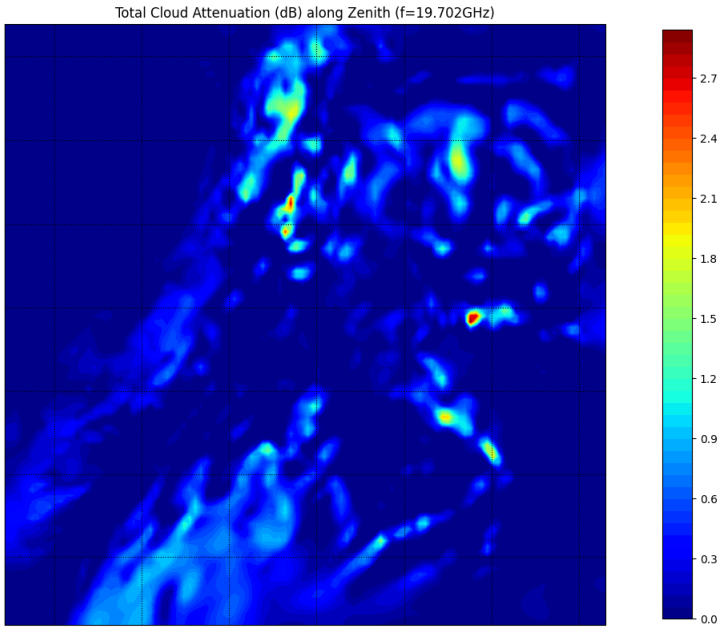

Figure 18: Zenithal Cloud Attenuation at f=19.702GHz

3.4 Raindrop Size Distribution

The raindrop size distribution (DSD) is the statistical distribution of the number of raindrops as a function of their diameter D. The processes that account for the formation of drops are three:

- Water vapour condensation
- Accumulation of small drops on large drops
- Collision between drops

In order to correctly account for attenuation caused by rain the DSD must be properly studied and defined.

The drop size distribution N_d is defined as the number of drops per unit volume, and is in general modeled as a truncated gamma function for diameter zero to a maximum possible size of rain droplets and is written as:

$$N_d\left(D_d\right) = N_{d,0} D_d^{\mu} \exp\left(-\Lambda_d D_d\right) \tag{65}$$

where D_d is the diameter of the drop, μ the shape factor and Λ_d the slope of the distribution. The most commonly used average distribution is given by Marshall-Palmer [7], which uses $N_{d,0} = 8 \times 10^6 \ m^3 m^{-1}$ and $\mu = 0$. The slope factor is strictly related to rain conditions [1], it is calculated in function of the liquid water content M:

$$\Lambda_d = \left[\frac{\pi \rho_w N_0 \Gamma\left(\mu + 4\right)}{6M}\right]^{\frac{1}{\mu+4}} \tag{66}$$

where ρ_w is density of water and Γ is the gamma function. The liquid water content is calculated from the WRF output for rain water mixing ratio Q_{RAIN} and air density ρ_{air}:

$$M = Q_{RAIN} \rho_{air} [g/m^3] \tag{67}$$

with ρ_{air} given as a function of pressure p:

$$\rho_{air} = \frac{p}{R_{spec} t} [g/m^3] \tag{68}$$

The following graph shows a Marshal and Palmer drop size distribution in accordance to rain water content.

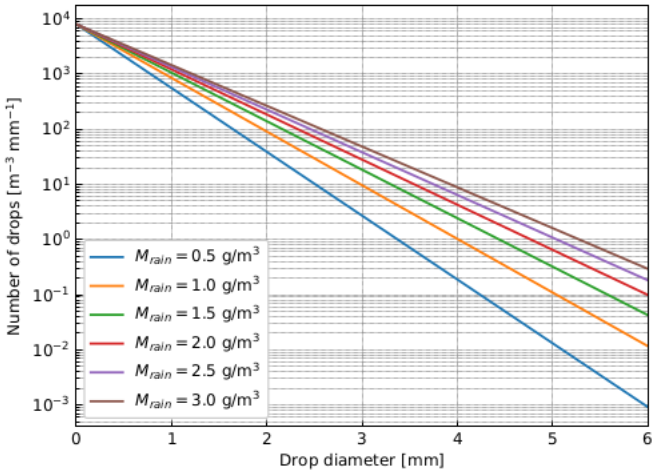

Figure 19: Liquid water content effect on rain drop size

By defining the terminal velocity as:

$$v\left(D_d\right) = 3.778 D_d^{0.67} \tag{69}$$

we are able to relate the particle size distribution to the rain rate in the following way:

$$R_{rain} = \rho_\omega \frac{\pi}{6} \int_0^\infty N_d\left(D_d\right) D_d^3 v\left(D_d\right) dD_d \times 3600 \tag{70}$$

Figure 20 shows an example of a small rain event with maximum rain rate of approximately 14 mm/h.

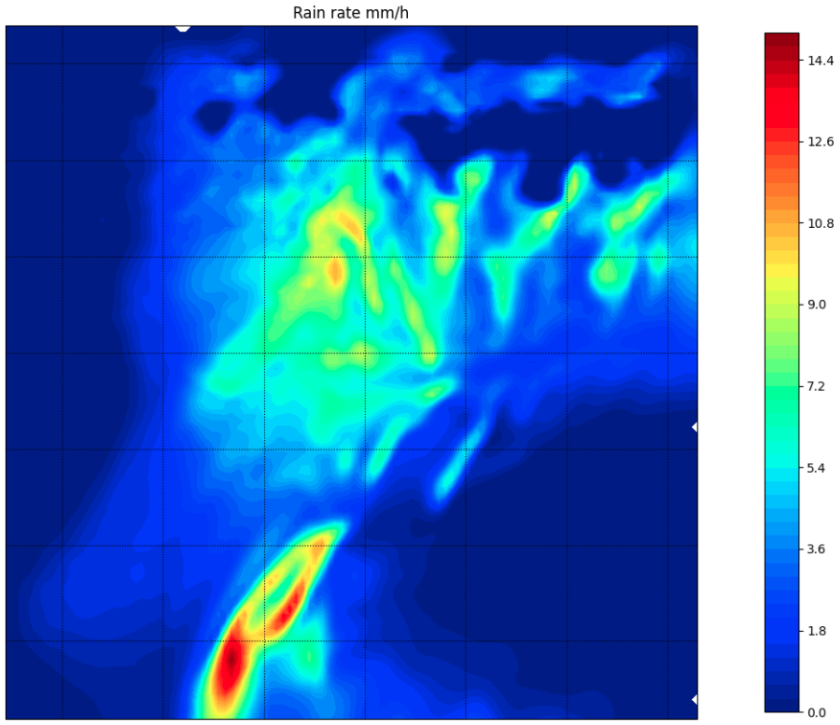

Figure 20: Rain rate on the 17th Of January 2015

3.5 Attenuation due to Rain

Rainfall is constituted by precipitating liquid hydrometeors, is characterized by a high temporal variability, in the range of seconds, and is divided spatially in two categories: stratiform rain, which extends on wide areas and presents weak precipitation rates (Rainfall rates), and convective rain, with a small spatial extension (in the range of few Km) and higher precipitation rates, so described by DSD with peaks on higher diameters, but also characterized by short temporal durations. In general rain attenuation mainly depends on Rainfall Rate R and DSD. The terminal fall velocities of droplets are in the range of 1-10 m/s, for diameters between 0.2 and 6 mm. Both rain categories contribute significantly to signal impairments, but while stratiform rain impact more on the temporal probability of exceedence of a certain attenuation threshold, convective rain bring such threshold to higher intensity levels.

With the assumptions made about the scattering properties of the hydrometeors and provided that the rainfall is spatially homogeneous over a propagation path the rain attenuation $A_{rain}(dB)$ can be expressed as a product of the specific

attenuation $\gamma(db/km)$ and path length $L(km)$:

$$A = \gamma L \tag{71}$$

The specific attenuation γ is related to the raindrop size distribution and the total extinction cross section:

$$\gamma = 4.343 \times 10^3 \int_0^{D_{max}} N(D)\sigma_e(D)dD \tag{72}$$

D_{max} is the diameter of the largest rain drop, usually considered at 4 mm, as any larger than this the drop tends to break up due to air resistance.

4 Methods for NWP data processing

4.1 Earth Coordinate Systems and Conversions

In order to successfully choose a reference system that takes into account all aspects of Earth-space links from NWP data some conversion must be made. The most common transformation is from Cartesian to spherical, however when considering the motion of satellites or the oblateness of the earth some further considerations must be made. The systems which are of interest are the Cartesian Earth-Centered Earth-fixed (ECEF) coordinates and the curvilinear Latitude and Longitude Altitude (LLA) coordinates, which are almost spherical and depend on how the earth is modeled: as an ellipsoid or geoid.

4.1.1 Cartesian and Spherical Coordinates.

Using right-handed Cartesian coordinates (x, y, z) the spherical coordinates (r, ϕ, θ) can be defined in the following way:

- r is the norm of the vector $\mathbf{r}$ from the origin to the point
- ϕ is the angle between the x axis and the projection of $\mathbf{r}$ on the xy plane
- θ is the angle between the projection of $\mathbf{r}$ on the xy plane and $\mathbf{r}$, or in the same way the complementary of the angle between the z axis and $\mathbf{r}$

Figure 21 shows how spherical coordinates and Cartesian coordinates are related.

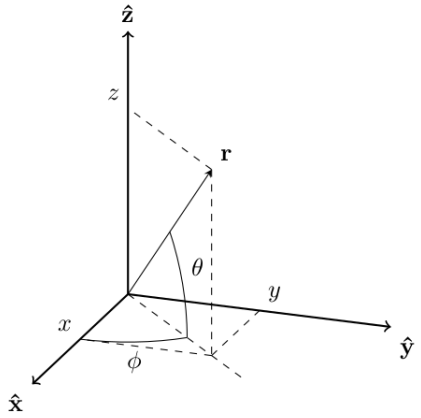

Figure 21: Spherical to Cartesian coordinates

where conversion between the two sets of coordinates are given by:

$$x = r\cos(\phi)\cos(\theta) \tag{73}$$

$$y = r\sin(\phi)\cos(\theta) \tag{74}$$

$$z = r\sin(\theta) \tag{75}$$

The conversion from Cartesian to spherical coordinates is given by:

$$r = \sqrt{x^2 + y^2 + z^2} \tag{76}$$

$$\phi = \arctan_2(y, x) \tag{77}$$

$$\theta = \arcsin\left(\frac{z}{x}\right) \tag{78}$$

4.1.2 Earth Global Non-Inertial Coordinates

To locate points on the surface of the Earth at a global scale by using a non-inertial frame it is necessary to have a reference which is rotating with Earth. This system is appropriate for geostationary satellites. These coordinates can be considered as the usual Latitude, Longitude and Altitude (LLA) coordinates found in geography. The corresponding Cartesian coordinates are the Earth-Centered Earth-Fixed (ECEF) coordinates whose frame of reference is defined by an x and y axis lying on Earth equatorial plane, with the z axis pointing towards the geographical North Pole, while x intersecting the Greenwich meridian. The way in which the LLA coordinates are described depend on how the Earth is modeled, as a sphere or as an ellipsoid of revolution. When Earth is modeled as a sphere we may use the equations from the previous section.

To describe an ellipsoid of revolution it is necessary to define the dimensions of the ellipse which is rotated during its construction. The semi-major axis a and semi-minor axis b along with the flattening f(ellipticity or oblateness) parameters are enough to fully describe the geometry:

$$f = 1 - \frac{b}{a} \tag{79}$$

Two other parameters, known as eccentricities are useful, and are defined as:

$$e = \sqrt{1 - \frac{b^2}{a^2}} \tag{80}$$

$$e^{'} = \sqrt{\frac{b^2}{a^2} - 1} \tag{81}$$

The volumetric mean radius R:

$$R = \sqrt[3]{ab} \tag{82}$$

Typical values for an Earth approximation are given by table 9, and are base on the World Geodetic System 1984 (WGS 84):

Table 9: Spherical Earth to Ellipsoid

Ellipsoid parameters	Spherical Earth	WGS 84
$f[/]$	0	$1/298.257223563$
$a[km]$	6371	6378.137
$b[km]$	6371	6356.752
$R[km]$	6371	6371.001
$e[/]$	0	0.08181919
$e_2[/]$	0	0.08209444

When Earth is modeled as an ellipsoid, that is with $a \neq b$, then latitude and altitude need to be redefined.

- h is the altitude and is defined as the shortest distance between the surface of the earth and a point
- φ is the geodetic latitude and describes the angle between the equatorial plane and the normal to the Earth surface at that point
- λ is the geodetic longitude
- $\varphi_s$the angle between the equatorial plane and the line r_s which connects the point's projection on the surface of the Earth to the center of the Earth

Given the previous definitions the LLA to ECEF conversion becomes:

$$x_{ECEF} = x_\lambda \cos(\lambda) \tag{83}$$

$$y_{ECEF} = x_\lambda \sin(\lambda) \tag{84}$$

$$z_{ECEF} = r_s \sin(\varphi_s) + h \sin(\varphi) \tag{85}$$

where x_λ is the projection of the position vector on the equatorial plane

$$x_\lambda = r_s \cos(\varphi_s) + h \sin(\varphi) \tag{86}$$

$r_s$is given by:

$$r_s = \frac{a}{\sqrt{1 + \left[\left(\frac{a}{b}\right)^2 - 1\right] \sin^2 \varphi_s}} \tag{87}$$

The conversion from ECEF to LLA can be done with:

$$\lambda = \arctan 2 \left(y_{ECEF}, x_{ECEF}\right) \tag{88}$$

and by an iterative approach starting from an approximation for φ:

$$\varphi \approx \arctan 2 \left(z, \frac{x_\lambda}{(1 - e^2)}\right) \tag{89}$$

and by using

$$\frac{\tan \varphi_s}{\tan \varphi} = \frac{b^2}{a^2} \tag{90}$$

and by introducing r_c

$$r_c = r_s \frac{\cos(\varphi_s)}{\cos(\varphi)} \tag{91}$$

we have

$$h = \frac{x_\lambda}{\cos(\varphi)} - r_c \tag{92}$$

φ can now be defined more closely to

$$\varphi = \arctan_2 \left(\frac{z}{r_{c(1-e^2)} + h}, \frac{x_\lambda}{r_c + h}\right) \tag{93}$$

A new iteration can be made to recalculate values for $r_c$and h. The procedure converges in few iterations, typically less than 6.

4.2 Slant Path Calculation Algorithm

Given the coordinates of the ground station and the geostationary satellite we are able to apply the algorithm which is used to evaluate the slant path and the involved pixels. To generate the total attenuation time series, it is necessary to integrate the specific attenuation associated to each pixel along the link slant path, which are individuated by knowing their azimuths, their elevations and their altitudes.

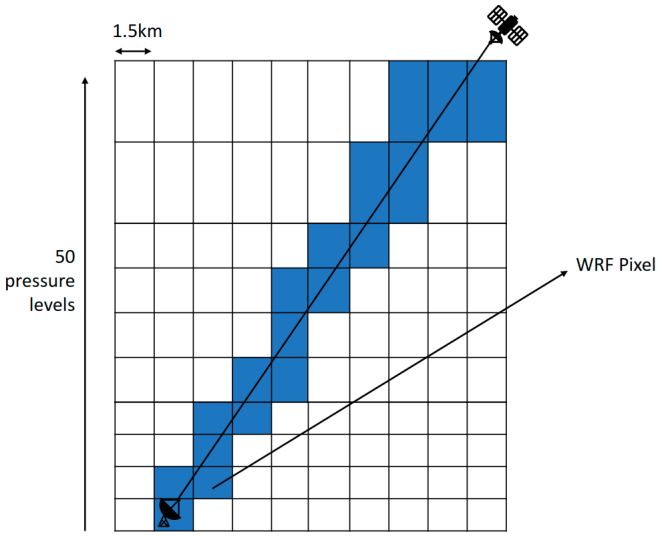

Figure 22: Slant Path Calculation

Given two points in 3-dimensional space defined by their spherical LLA coordinates:
$\widehat{\mathbf{P}}_{sta}\,(r_{sta}, lon_{sta}, lat_{sta})$ and $\hat{\mathbf{P}}_{sat}\,(r_{sat}, lon_{sat}, lat_{sat})$ where:

- r_{sta} is given by

$$r_{sta} = r_{earth} + h_{spino}$$

where $r_{earth} = 6371000$ m is Earth's average radius and $h_{spino} = 86$ m is Spino d'Adda's receiver height from sea level.

- lon_{sta} and lat_{sta} are Spino d'Adda's WGS longitude and latitude coordinates

$$lon_{sta} = 9.494425^{\circ}E$$

$$lat_{sta} = 45.413168^{\circ}N$$

For the geostationary satellite we have:

- $r_{sat} = 35786000$ which is the distance from the center of the Earth to the orbit
- $lon_{sat}$and lat_{sat} are the satellite's WGS longitude and latitude coordinates

$$lon_{sta} = 25°E$$

$$lat_{sta} = 0°N$$

The first step is the conversion from LLA to ECEF coordinates, by following the equations given in the previous section is straightforward. We obtain the Cartesian coordinates $P_{sta}\left(x_{sta}, y_{sta}, z_{sta}\right)$ and $P_{sat}\left(x_{sat}, y_{sat}, z_{sat}\right)$

The distance between the two points is given by

$$dist = \sqrt{\left(x_{sta} - x_{sat}\right)^2 + \left(y_{sta} - y_{sat}\right)^2 + \left(z_{sta} - z_{sat}\right)^2} \tag{94}$$

and the line equation written in vector form:

$$P\left(x, y, z\right) = \left(x_{sta}, y_{sta}, z_{sta}\right) + \tau\Gamma \tag{95}$$

where Γ is the direction vector:

$$\Gamma = \left(\left(x_{sta} - x_{sat}\right), \left(y_{sta} - y_{sat}\right), \left(z_{sta} - z_{sat}\right)\right) \tag{96}$$

and τ is a scalar variable which indicates line progression and is therefore bound from 0 to 1. This parameter is key when defining the level of resolution in which to consider the slant path. When resolution is set at intervals of 15 m $\Gamma = 3.93317721 \times 10^{-7}$.

The algorithm works iteratively by increasing τ in the line equation, finding the new Cartesian coordinates $P_{new}\left(x_{new}, y_{new}, z_{new}\right)$ and calculating r_{new},which is the distance of P_{new} from the center of the Earth. In order to place P_{new} within the closest pixel the height from sea level must be calculated as $h_{new} = r_{new} - r_{earth}$.

The conversion from Cartesian to spherical LLA coordinates are done with the aforementioned formula.

From $\hat{\mathbf{P}}_{new}\left(r_{new}, lon_{new}, lat_{new}\right)$ we are now able to convert the LLA coordinates into the indeces of the pixel which $\hat{\mathbf{P}}_{new}$ belongs to.

The number of instances that the pixel generates translates into the total distance crossed within that pixel. To obtain the total distance traversed by the signal in any box the "total_count" value is multiplied by the step sequence resolution, either 15 o 50 m.

5 Code Implementation

5.1 Libraries and Code Dependencies

This section gives a brief overview of the implemented Python code. A selection of libraries and dependencies are necessary to run the software.

Table 10: Python libraries used in implementation

Library	Description
Numpy	Array computing
Xarray	N-D labeled arrays and datasets
Scipy	Numerical routines integration and optimization
Cython	Compiler for writing C extensions
Cftime	Time-handling functionality for netcdf
Matplotlib	Python plotting package
H5netcdf	Python interface for the netCDF4 file-format
gfortran	GNU Fortran compiler
WRF-python	Diagnostic and interpolation routines for WRF data
Pytmatrix	T-matrix scattering computations
netcdf	Object-oriented python interface to the netCDF library
Cartopy	Maps for data analysis and visualisation

Due to the size of the data for the two months, totaling approximately 1,6 TB an iterative approach was used. The code works by ingesting one hour's worth of data, and processing that data one minute at a time, in order to obtain a minute by minute estimation of attenuation from the WRF data.

The implementation of the Python code runs on 6 modules, the relationship of which is shown in figure 23. Data used as input/output are shown as cylindrical databases and modules are rectangular. Before running the code some basic inputs are required from the user, such as signal frequency and time period of the analysis.

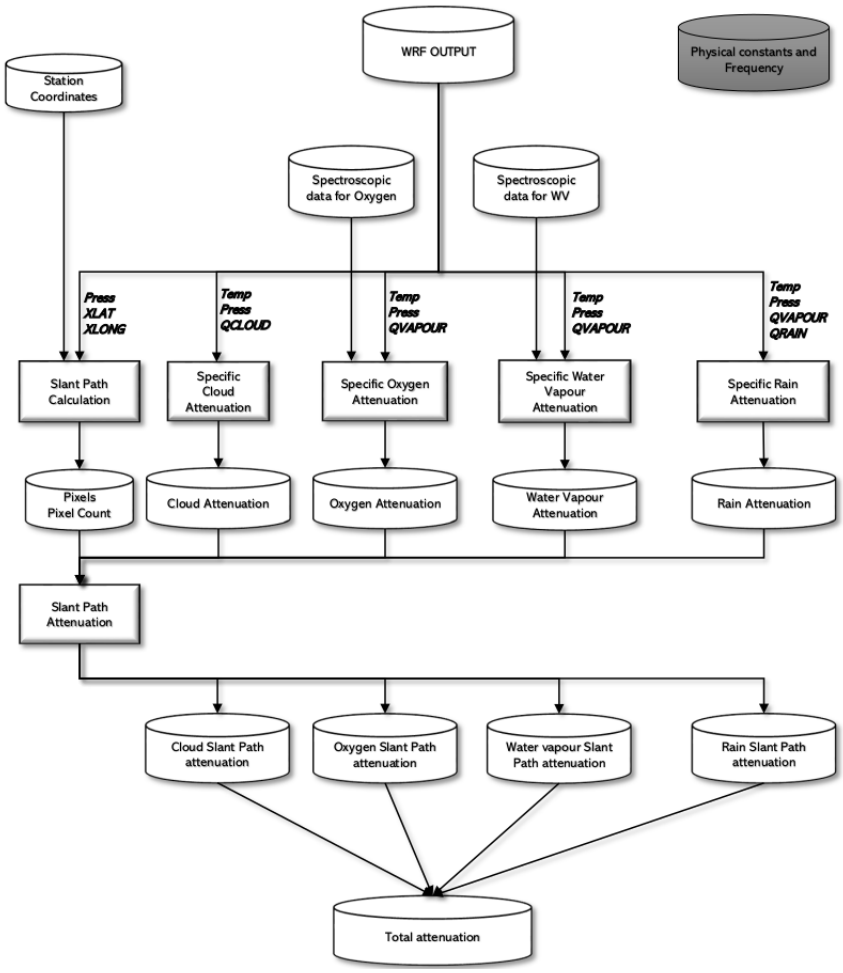

Figure 23: Data and module dependency

5.1.1 Slant Path Calculation Module

As seen in the in figure 23 and chapter 4.2, the slant path module takes as input the ground station and the satellite coordinates, along with the latitude and longitude and pressure information from the WRF data. The pressure taken as input is used to calculate the height from the geopotential as seen in equation 1. The module makes use of a function from the WRF Python library, wrf.ll_to_xy, which converts latitude and longitude coordinates into matrix indeces in order to proceed with array calculations. The height matrix index is obtained through a function that takes as input all heights at the new coordinates and "snaps" the index value to closest value. During a long term run (week or month) analysis of WRF data the slant path module is called only

once every hour or day to optimize computation time, as running the function every minute adds a negligible accuracy, pressure levels are stable with respect to such time periods.

A further change can be made to reduce computation time, as mentioned previously, by changing the step resolution along the slant path, i.e. from 15 m to 50 m.

The output of the module comes in the form of two arrays. 'Pixels' records which pixels have been traversed, 'Pixel Count' tells us how many times the step function "landed" in that pixel, which along with the step resolution is used to calculate the total distance in meters in the pixel itself.

5.1.2 Specific Cloud Attenuation Module

The cloud attenuation module takes as inputs, the temperature (K), pressure (Pa) and QCLOUD (kg^{-1}/kg^{-1}), along with and other physical constants mentioned in section 3.3. The input and output data maintain the same shape and operations are done across all pixels, that is for 49 x 108 x 108 in space across the 60 minute time interval.

5.1.3 Specific Oxygen and Water Vapour Attenuation Modules

The two modules both take as input the same WRF data, the temperature (K), pressure (Pa) and QVAPOUR (kg^{-1}/kg^{-1}), along with signal frequency and spectroscopic data. As with the cloud module the input and output data maintain the same shape and operations are done across all pixels, that is for 49 x 108 x 108 in space across the 60 minute time interval. However for every minute a further iteration must be done for the line shape factor over the spectroscopic data, which adds an additional 48 iterations for Oxygen and an additional 34 for water vapour.

5.1.4 Specific Rain Attenuation and Rain Rate Module

This module is the most computationally expensive as it requires integration across all pixels and drop sizes. It take as input the temperature (K), pressure (Pa), QVAPOUR (kg^{-1}/kg^{-1}) and QRAIN(kg^{-1}/kg^{-1}) along with signal frequency, and other physical constants mentioned in section 3.3 for the calculation of the complex refractive index. This module makes use of the Pytmatrix [19] for the generation of the scatterer object, which takes as input:

- *wavelength*
- *radius*
  - The radii of the drops were considered from 0.1 to 4 mm
- *refractive index,* the complex refractive index of the scatterer
  - Obtained through the equations in section 3.3

- *axis ratio,* the horizontal-to-rotational axis ratio
  - Obtained through a function based on Beard and Chuang's "A New Model for the Equilibrium Shape of Raindrops"[10]

and is used to extract the attenuation cross section of the drop, by using pytmatrix.ext_xsect().

The same module can also output the rain rates using the two methods reported in the previous chapters. The first method uses the accumulated rain values and through equation 10 we obtain figure 24. While the second method uses the DSD and equation 70, resulting in the values reported in figure 25.

The two methods result in very similar values, however at a computational level the first method is much faster, as there is no need to integrate across drop sizes. The first method is used to identify rainy periods during the computation of rain attenuation. Rainy periods are identified by a flag in order to avoid unnecessary calculations of non-rainy periods.

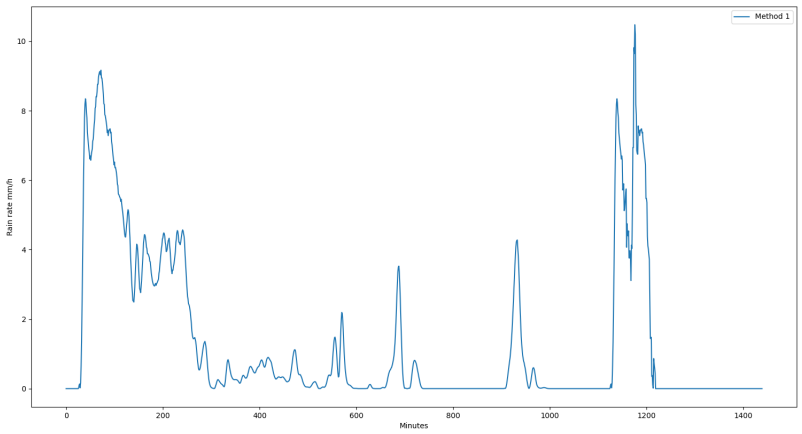

Figure 24: Rain Rate January 17th 2015, Method 1

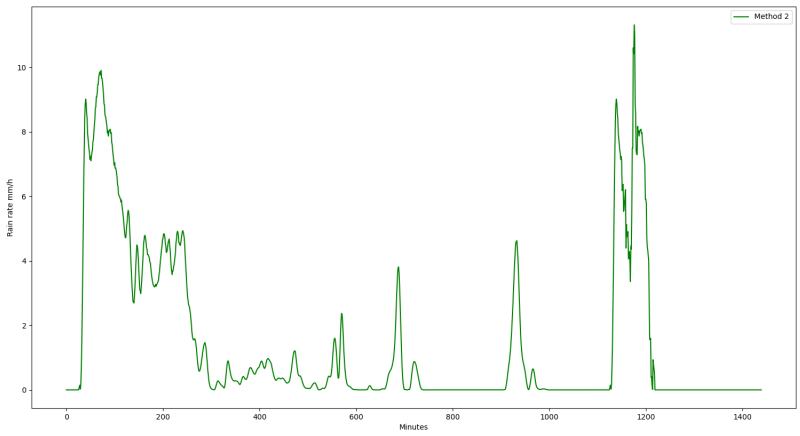

Figure 25: Rain Rate January 17th 2015, Method 2

5.1.5 Slant Path Attenuation Module

This module converts specific attenuation levels (dB/km) into absolute attenuation levels (dB). For every minute, the attenuation along the path is calculated by summing the attenuation of each pixel. The attenuation of each pixel is obtained by multiplying the specific attenuation of that pixel by the number of meters traversed by the signal in the pixel under consideration. The output is therefore no longer a matrix but an array of values for the attenuation for the whole hour for each tropospheric contribution. The total attenuation is therefore the sum of these values.

5.1.6 Final Remarks

The computation over a long-run can be parallelized across a multiprocessor in order to reduce computation time. Parallel processing was accomplished by splitting the period into sets of smaller groups of days and running the computation simultaneously. The output is reorded and saved into a csv file for further post processing and plotting.

Over the period of 2 months more than 87840 WRF files were analyzed. Among these a small amount of files were either incomplete or corrupt causing delays in long run computation runs. It was necessary therefore to locate and replace the existing files with a duplicate from either the previous or subsequent minute. This operation was done a total of 14 times across the 2 months of data. The 6th of January was missing approximately 50% of its data, at fairly predictable intervals. An interpolation between the values was done in order to restore the file to be used by the software.

6 Results

First, the results in terms of instantaneous attenuation values are studied against typical tropospheric phenomena. Then a comparison is done between the time series attenuation obtained from the software introduced in the previous section with the WRF data, and the data recorded from the ASI ground station in Spino d'Adda. Finally a statistical analysis through the use of Complementary Cumulative Distribution Functions (CCDF) is done in order to design the trospopheric margin for a given system availability.

6.1 Attenuation Values

6.1.1 Instantaneous Attenuation Values

Figures 26, 27 and 28 present the specific attenuation for water vapour, Oxygen, clouds and rain at an altitude of approximately 2 km. At the higher altitude of 20 km the components of the tropospheric attenuation reach negligible values compared to the level of attenuation in figures 26, 27 and 28. In particular the attenuation due to rain, fog and cloud are equal to zero while the amplitude of the gaseous attenuation decreases by a factor 10^3 for Oxygen and 10^6 for the water vapour as seen in figures 29 and 30. The gaseous attenuation decreases with altitude while the attenuation due to rain and clouds are bounded below 5 km height for these specific events as seen in figure 31. These results validate the assumption that the attenuation due to Oxygen and water vapour is negligible above 20 km height. The attenuation due to rain and clouds is limited in altitude by the altitude of the clouds.

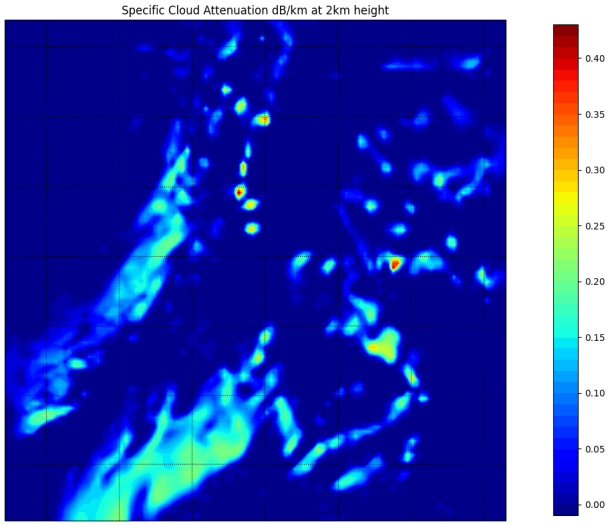

Figure 26: Specific attenuation for clouds at a height of 2km

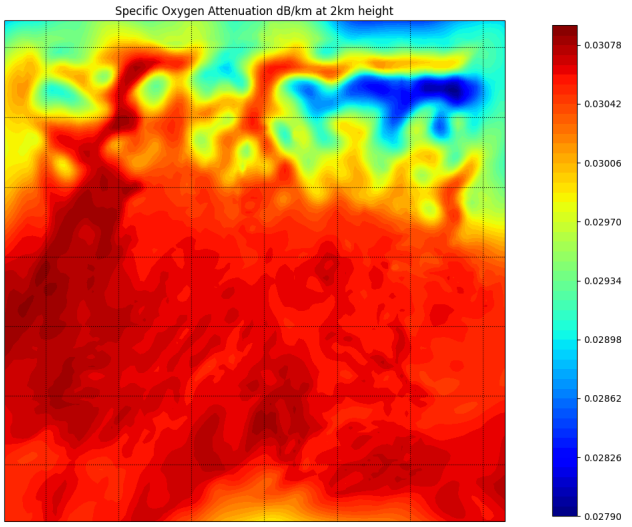

Figure 27: Specific attenuation for Oxygen at a height of 2km

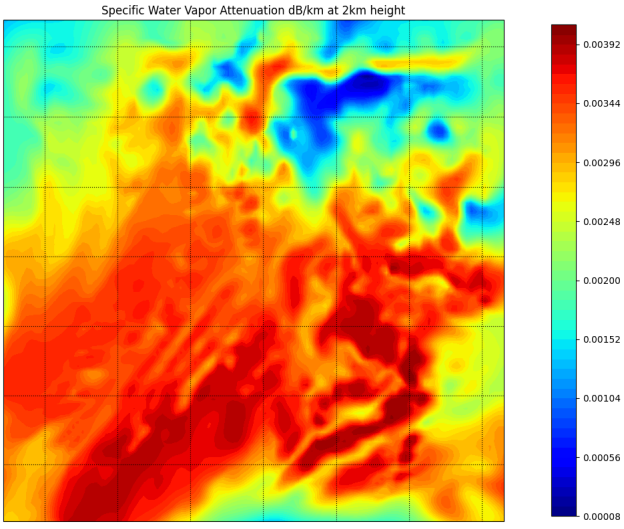

Figure 28: Specific attenuation for Water Vapour at a height of 2 km

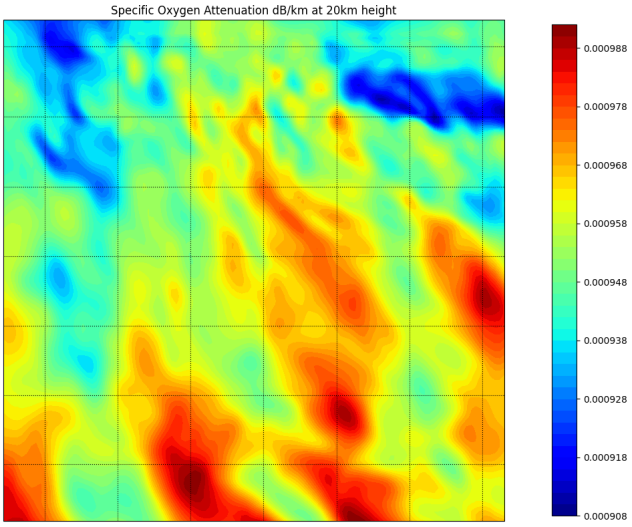

Figure 29: Specific attenuation for Oxygen at a height of 20 km

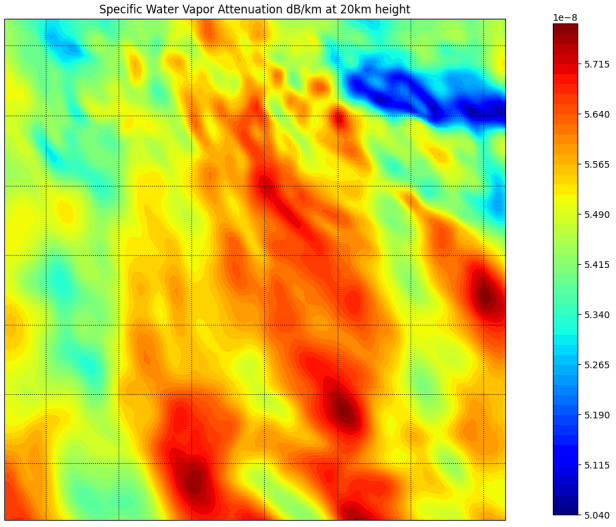

Figure 30: Specific attenuation for Water Vapour at a height of 20 km

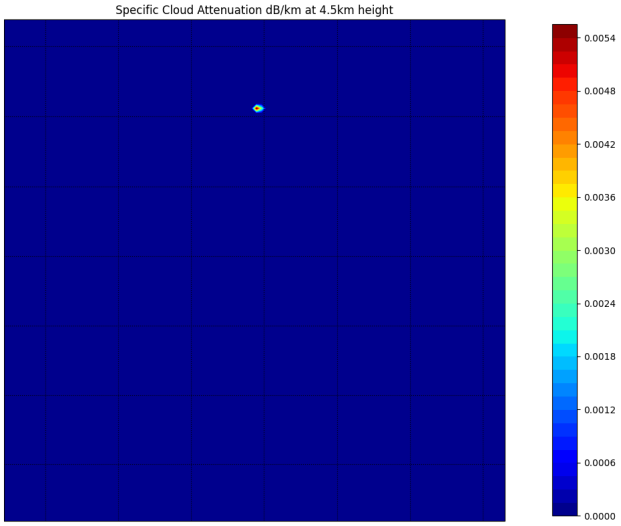

Figure 31: Specific attenuation for clouds at a height of 4.5 km

6.1.2 Monthly Attenuation Values

The results reported in this section focus on two months of WRF data, January and June 2015. These months were selected because of the different meteorological conditions, from clear skies to heavy rain. Figures 32 and 33 show the recorded data from the ASI ground station with the experimental set-up presented in section 2.3 and the total attenuation calculated through WRF data and across the whole month of January at the beacon frequency of f=19.701GHz.

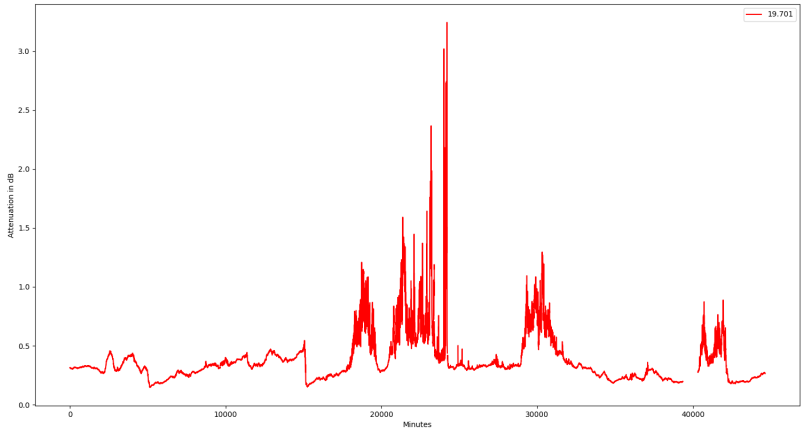

Figure 32: Total attenuation for Spino d'Adda ground station at $f = 19.701GHz$, January 2015

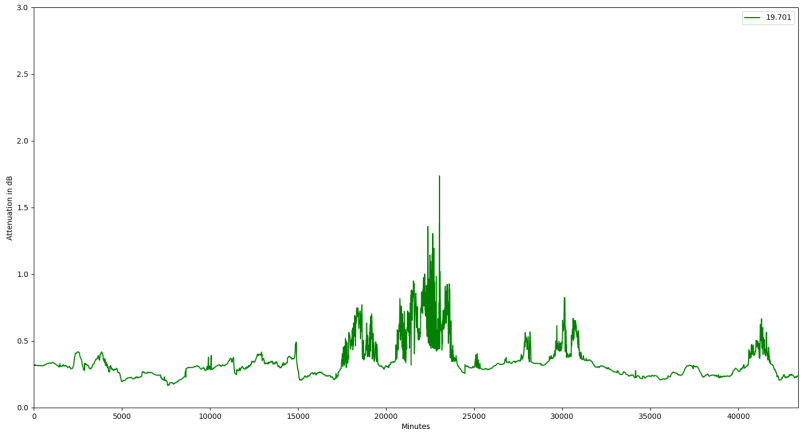

Figure 33: Total monthly attenuation from WRF data at $f = 19.701GHz$, January 2015

Figures 34 and 35 show the results for the month of June, which was characterized by much more variable weather conditions with respect to January, which only had one significant rain event on the 17th. June was characterized by 7 rain events of different intensities.

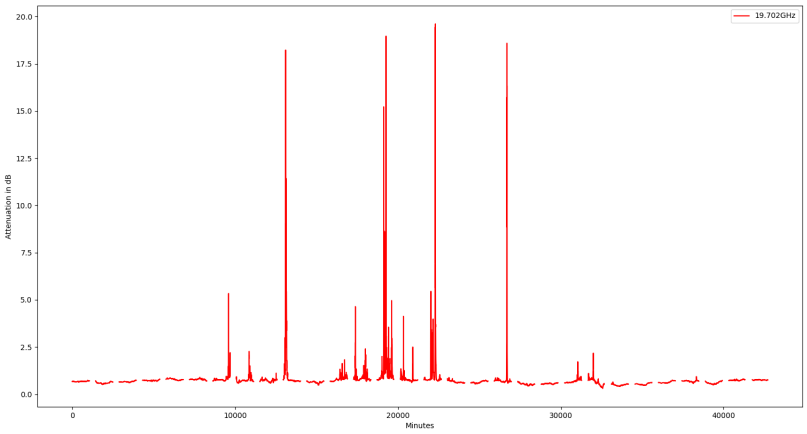

Figure 34: Total attenuation for Spino d'Adda ground station at $f = 19.701GHz$, June 2015

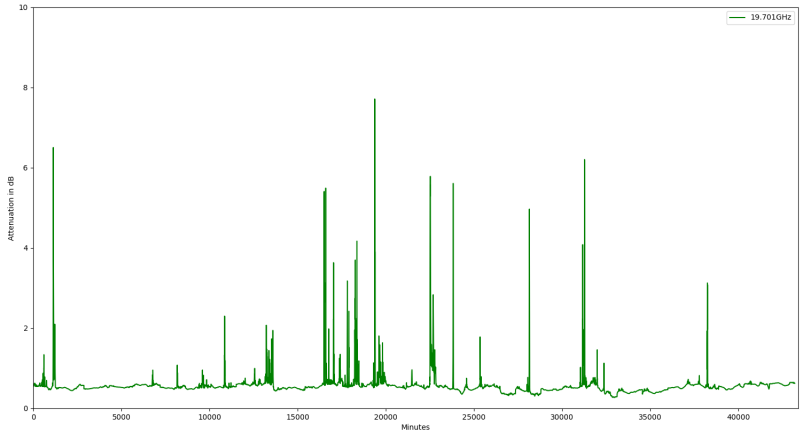

Figure 35: Total monthly attenuation from WRF data at $f = 19.701GHz$, June 2015

Figure 36 and 37 show the attenuation contribution levels due to rain, cloud, oxygen and water vapour across January and June respectively. The gaseous attenuation depends on the meteorological conditions, but it can be noticed that the variations of the gaseous components are lower compared to the other contributions.

Oxygen is very stable while the contribution from water vapour fluctuates slowly during the course of the day and the month, it is still relatively predictable compared to the contribution of cloud and rain. When designing a telecommunication link, the gaseous contribution is always present, while attenuation due

to rain and clouds are intense events undergoing very strong variations in time. Thus the power required to guarantee the signal to noise ratio at the receiver is higher, if all meteorological conditions are considered.

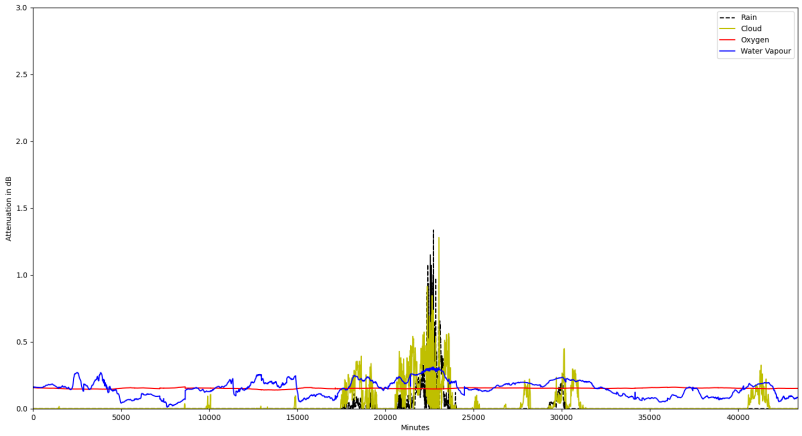

Figure 36: Contribution of Cloud, Rain, Oxygen and Water vapour across the month of January 2015, $f = 19.701GHz$

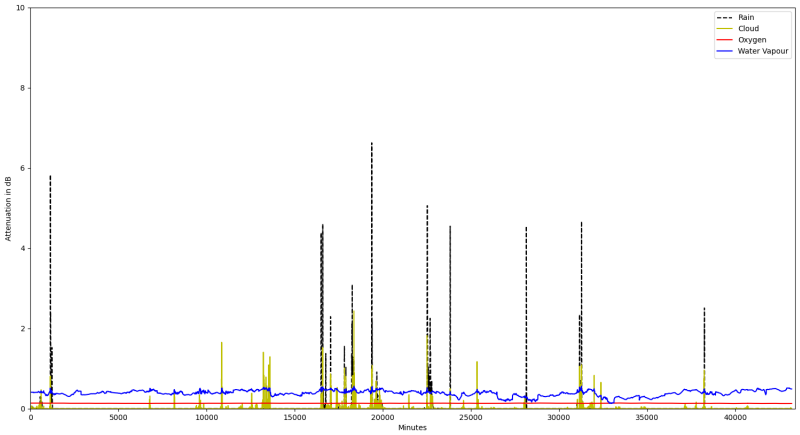

Figure 37: Contribution of Cloud, Rain, Oxygen and Water vapour across the month of June 2015, $f = 19.701GHz$

While June clearly shows much more variable weather conditions with respect to January, we can also notice a clear difference in average overall attenuation, this is due to the gaseous part of the attenuation. The behaviour with respect to increasing temperature is opposite for the two gases: while Oxygen attenuation decreases, water vapour increases at a faster rate, meaning that in

the hotter month of June gaseous attenuation is more than double the amount of colder days in January. Figure 38 clearly shows this difference.

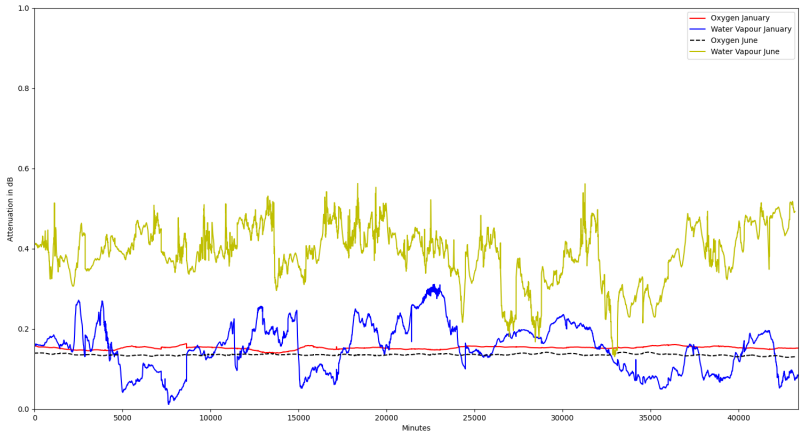

Figure 38: Water vapour and Oxygen Attenuation, January and June 2015, $f = 19.701GHz$

6.1.3 Daily Attenuation Values

Figures 39, 40 and 41 present the superposition of the attenuation derived from the WRF data and the data from the ASI ground station for a clear day, for a cloudy day and a rainy day respectively. The relative difference between the prediction and the measurement is negligible and thus is a good prediction of the attenuation for clear days. For cloudy and rainy days, the WRF predictions show the same range of attenuation values observable from measurements, however the peaks due to the rain events from the WRF predictions and the measurements struggle to match in time. The levels for rain events computed with WRF are highly sensitive to the ground station position: a shift of few kilometers can lead to strong variations in the values.

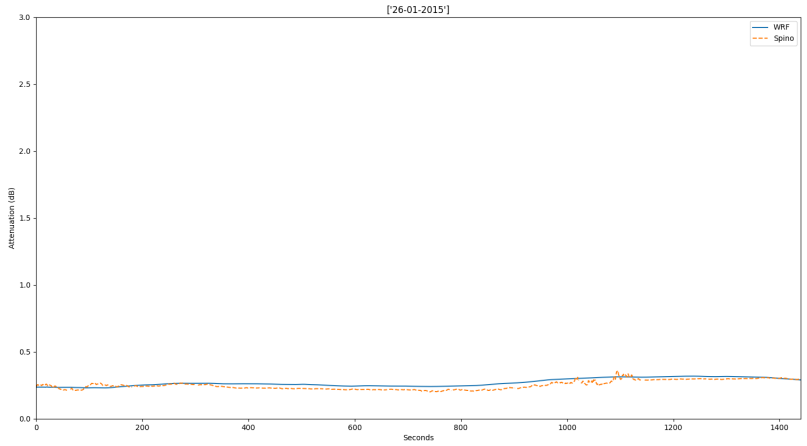

Figure 39: Clear day attenuation due to gases. 26th January 2015, $f = 19.701GHz$

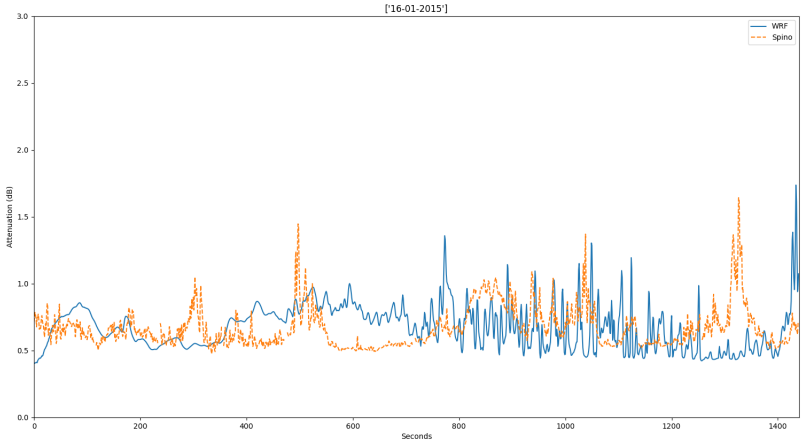

Figure 40: Cloudy day attenuation 16th January 2015, $f = 19.701GHz$

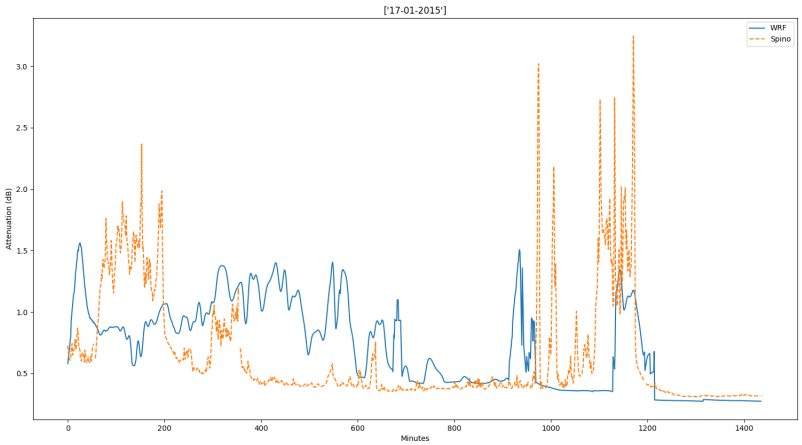

Figure 41: Rainy day attenuation 17th January 2015, $f = 19.701GHz$

The rain rate recorded on the 17th of January by the ASI ground station has two clear rain events and are shown in figure 42. The WRF rain rate prediction is shown in figure 43. The first rain event recorded by the ground station begins approximately one hour after the WRF and finishes about an hour earlier than the WRF prediction. The average rain rate is below that of the WRF data. The second rain event recorded by the ground station is very short, but rather intense, reaching a maximum of 35 mm/h. WRF data seems to show less intense but broader rain events. The amplitude of the precipitations is strongly different between the measurement and the prediction. This difference can be explained by the localized nature of the precipitations. Indeed the rain events are limited in space and can undergo strong variations as it can be seen on the figure 20, moreover this difference might be due to the limited accuracy of the meteorological prediction obtained from the WRF simulation under $1.5km^2$, which is the horizontal resolution of the WRF data as seen in chapter 2.

The accumulated rain amount can also help understand the difference between the predicted and recorded data. Figure 44 shows a comparision in accumulated rain amount across the 17th of January. The first rain event for the WRF data is less intense but lasts longer in time, accumulating much more rain than the recorded data over the same period of time.

However we can clearly see from figure 41 that rain attenuation matches in time the rain rate. In order to evaluate the risk of exceeding a certain value of attenuation a statistical approach is preferred and will be studied in section 6.2. While January 17th shows fairly good results in terms of predicted and recorded rain data, other days do not have nearly as much precision. For instance, figure 45 shows predicted and recorded rain rate on the 14th of June. Not only are the values different in terms of amount and time, but the second rain event of the day is not predicted by the WRF data.

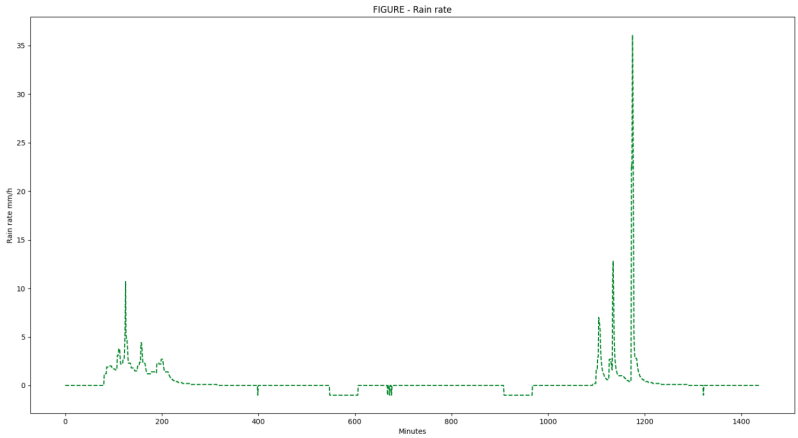

Figure 42: Rain Rate January 17th 2015, ASI Spino d'Adda data

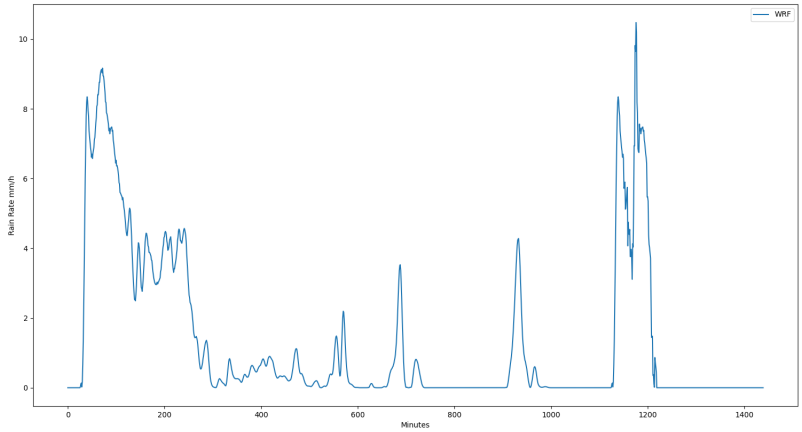

Figure 43: Rain Rate January 17th 2015, WRF Data (method 1)

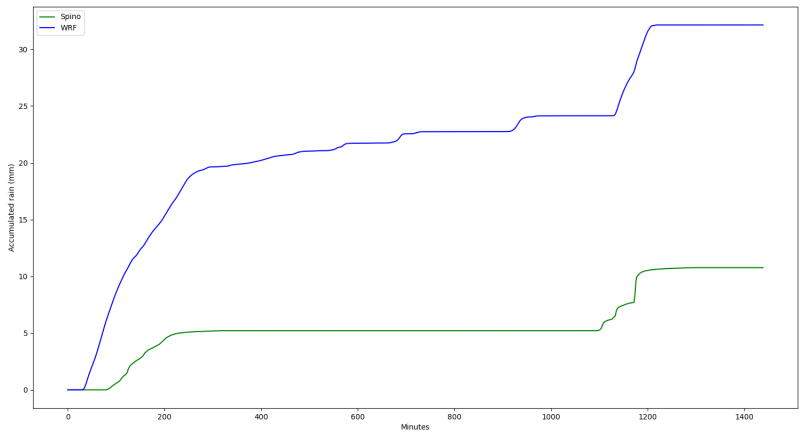

Figure 44: Accumulated Rain Amount January 17th 2015

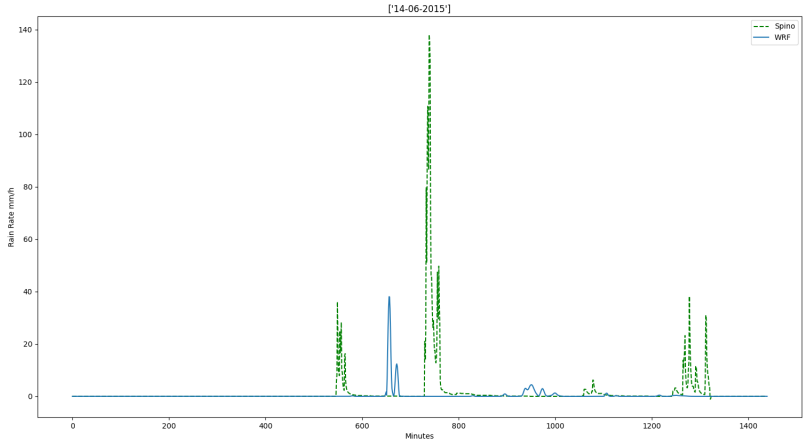

Figure 45: Rain Rate June 14th 2015

6.2 Statistical Approach

The statistical analysis is performed over two months so that the CCDF can be used to identify the power margin to guarantee the correct operation of the link in the associated time slot, i.e. to meet the target availability time; Figures 46 and 47 present the CCDFs for the simulation periods. The results are overall satisfactory, there is a slight underestimation of WRF generated attenuation with respect to the measured values. This is due to the contribution of clouds and, more heavily, to the contribution of rain, for which there is a strong underestimation with respect to the peaks shown in the recorded data seen in the previous section. The CCDF over the entire 2 month period is shown

in figure 48.

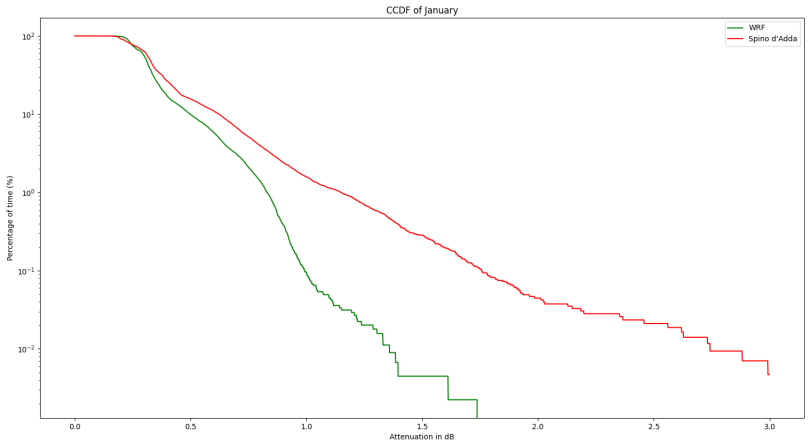

Figure 46: CCDF for January at $f = 19.701GHz$

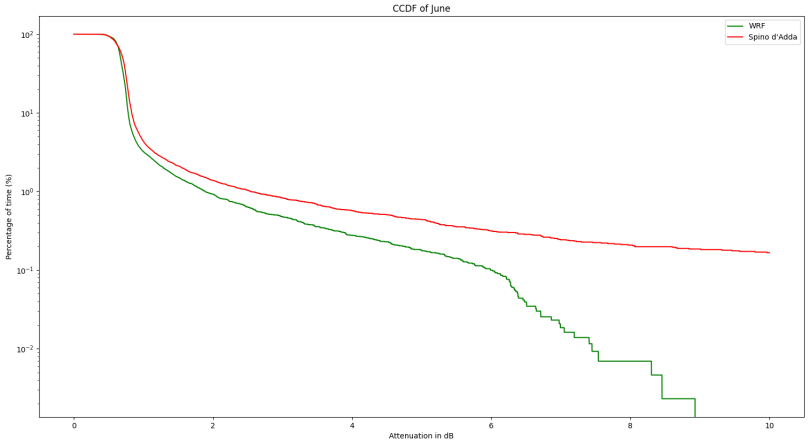

Figure 47: CCDF for June at $f = 19.701GHz$

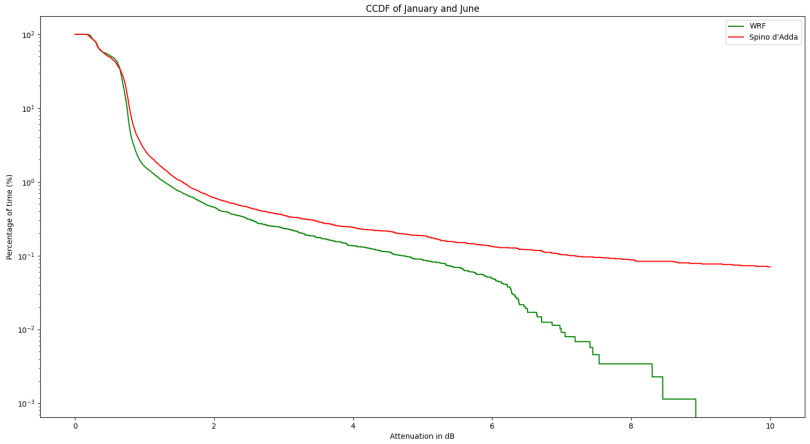

Figure 48: CCDF January and June at $f = 19.701GHz$

Regarding rain rate, figure 49 shows the CCDF over the studied period. The results obtained are inline with what has been stated in the previous section. The WRF rain events are much broader in time, the CCDF therefore results in a larger percentage of time spent over certain rain rates. The CCDF shown in figure 50 is taken from a single rainy day on the 17th of January. Here it is clear that strong peaks over a certain threshold are recorded by the ground station, which are not reported in the WRF data.

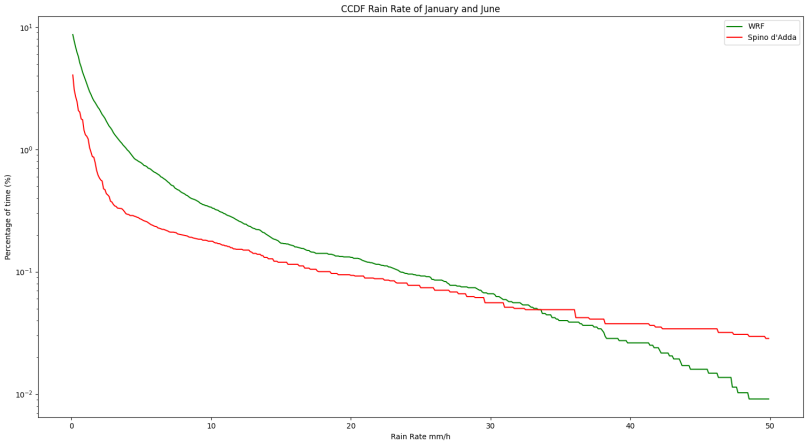

Figure 49: CCDF Rain rate January and June

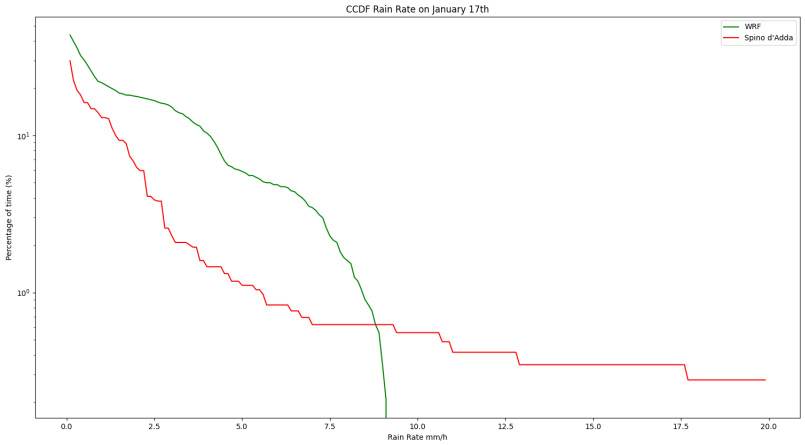

Figure 50: CCDF Rain rate January 17th

7 Final Remarks

The study conducted in this thesis has led to the characterization and prediction of the tropospheric attenuation for high frequency Earth-space links using WRF, which is a data set obtained through a high resolution Numerical Weather Prediction model. Specifically, the link between the Alphasat satellite and the ASI ground station located in Spino d'Adda was studied at the beacon frequency of 19.7GHz.

Starting from the WRF data, and following the ITU-R Recommendations, the specific cloud, rain and gaseous attenuations were computed across all pixels over the months of January and June 2015. Then by calculating the slant path between the ground station and satellite, minute-by-minute attenuation values were obtained and tested against the ground station recorded data. Post processing analysis and various data plots were done in order to correctly compare the two data sets. The software implementation of this was done in Python.

The following conclusion can be made:

- The prediction of the attenuation using the WRF simulation provides reliable results for clear sky conditions. It means that the attenuation due to oxygen and water vapour are well predicted.
- Cloud attenuation is well defined in terms of peak value attenuation, but the time series analysis shows a limited agreement between predictions and measurements
- The simulation does not provide very reliable predictions for the attenuation due to rain. The level of predicted rain attenuation is lower compared to the measured attenuation. Moreover the attenuation peaks due to the rain events from the WRF predictions and the measurements struggle to match in time. The direct exploitation of the predictions as a function of time is not reliable for precisely identifying the level of attenuation undergone by the link. However a statistical analysis can provide a more reliable basis to evaluate link availability.

The total attenuation values reached are slightly lower when compared to the ground station measurements. Attenuation due to rain is usually the highest type of attenuation, when using the WRF dataset, rain attenuation is not high enough. This causes the total attenuation to be lower than expected.

To conclude this work, it can be said that the WRF dataset can be used to estimate cloud and gaseous attenuation. However, the rain attenuation is underestimated. Future work includes investigating the impact of space and time resolution on the WRF predictions and the analysis of the estimated attenuation in an area around the ground station.

Acknowledgements

Acknowledgements go to CIMA Research Foundation for providing WRF data and to ASI for funding and supporting the Alphasat Aldo Paraboni experiment.

References

[1] (Cianca, Rossi, Yahalom, Pinhasi, Farserotu, Sacchi, 2011) EHF for Satellite Communications: the New Broadband Frontier

[2] (Reid, Neish, Walter, Enge, 2016) Leveraging Commercial Broadband LEO Constellations for Navigation

[3] (Khan, 2015) Mobile Internet from the Heavens

[4] (T. Grimwood, 2016) Union of Concerned Scientists Satellite Database. http://www.ucsusa.org/nuclear-weapons/space- weapons/satellite-database

[5] (García, Jeannin, Féral, Castanet, 2013). Use of WRF Model to Characterize Propagation Effects in the Troposphere

[6] (ITU, 2017) ITU (2017). ITU-R Recommendations. Standard, Radiocommunication Sector of the ITU

[7] (Marshal, Palmer, 1948). The distribution of raindrops with size. Journal of Meteorology.

[8] (Mie, 1908). Beiträge zur Optik trüber Medien, speziell kolloidaler Metallösungen An- nalen der Physik. Vierte Volge, Band 25.

[9] (Van de Hulst, 1981) Light scattering by small particles. Dover Publications.

[10] (Beard, Chuang, 1987) A New Model for the Equilibrium Shape of Raindrops.

[11] (Ippolito, 1981) Radio Propagation for Space Communication Systems.

[12] ITU-R. (2019). Recommendation ITU-R P.676-12, Attenuation by atmospheric gases and related effects.

[13] ITU-R. (2019). Recommendation ITU-R P.840-8, Attenuation due to clouds and fog.

[14] McGraw-Hill. (2009). Troposphere, Concise Encyclopedia of Science and Technology.

[15] (Codispoti, Luini, Parca, Ruggieri, Rossi, De Sanctis, Riva, 2018) The role of the Italian Space Agency in investigating high frequencies for satellite communications: The Alphasat experiment.

[16] (Riva, Luini, D'Amico, Nebuloni, Marziani, Consalvi, Marzano, 2018) The Alphasat Aldo Paraboni propagation experiment: Measurement campaign at the Italian ground stations.

[17] (Laurent Quibus, 2020) Modelling propagation impairments of Earth-Space links using Numerical Weather Prediction tools.

[18] (Ray, 1972) Ray, P. S. (1972). Broadband complex refractive indices of ice and water.

[19] (Leinonen J.) Python code for T-matrix scattering calculations. Available at https://github.com/jleinonen/pytmatrix/

[20] Weather Research & Forecasting Model, https://www2.mmm.ucar.edu/wrf/

[21] https://www.cimafoundation.org/foundations/research-development/wrf.html

[22] (Mischchencko, Travis, Mackowski, 1996) T-Matrix Computatios of Light Scattering By Non-Spherical Particles

[23] (Gunn, East, 1954) The microwave properties of precipitation particles